Materials and Design 186 (2020) 108235

Contents lists available at ScienceDirect

Materials and Design

journal homepage: www.elsevier.com/locate/matdes

On the size and orientation effect in additive manufactured Ti-6Al-4V

D. Barba [a,b,*], C. Alabort [c], Y.T. Tang [b], M.J. Viscasillas [a], R.C. Reed [d,b], E. Alabort [e]

[a] *Escuela Técnica Superior de Ingeniería Aeronáutica y Del Espacio (ETSIAE), Universidad Politécnica de Madrid, Plaza Cardenal Cisneros 3, 28040, Madrid, Spain*
[b] *Department of Materials, University of Oxford, Parks Road, Oxford, OX1 3PH, United Kingdom*
[c] *School of Industrial Engineering, Universitat Politècnica de València, Camino de Vera, 46022, Valencia, Spain*
[d] *Department of Engineering Science, University of Oxford, Parks Road, Oxford, OX1 3PJ, United Kingdom*
[e] *OxMet Technologies, Unit 15, Oxford Industrial Park, OX5 1QU, United Kingdom*

HIGHLIGHTS

- The specimen size and orientation effect on strength and ductility of additive manufactured Ti-6Al-4V is rationalised.
- Our results show systematic strengthening and a drastic drop in ductility as the material section is reduced.
- These changes are rationalised and linked to changes in microstructure, chemistry, and surface quality.
- Strengthening is due to combined changes in α-lath thickness, oxygen enrichment, and prior-β grain size.

GRAPHICAL ABSTRACT

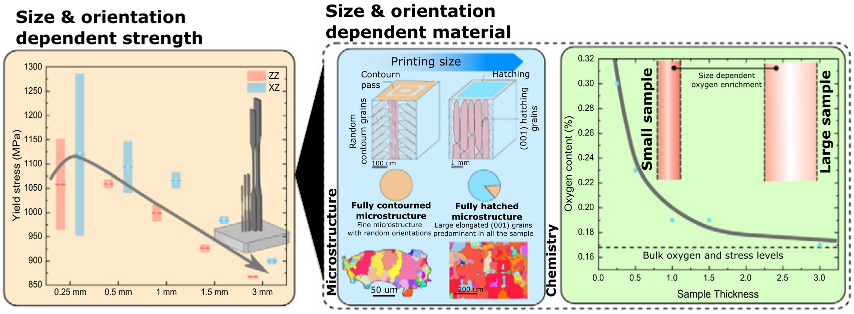

ARTICLE INFO

Article history:
Received 8 June 2019
Received in revised form 14 September 2019
Accepted 24 September 2019
Available online 1 November 2019

Keywords:
Titanium
3D printing
Strength
Experimental mechanics
Additive

ABSTRACT

In this work, the influence of the specimen size and orientation on the strength and ductility of additive manufactured Ti-6Al-4V is analysed and rationalised in a complete framework. First, the mechanical properties are addressed – as a function of surface-type, orientation, and size. Our results show systematic strengthening and a drastic drop in ductility as the material section is reduced. These changes are rationalised and linked to changes in microstructure, chemistry, and surface quality. Strengthening is due to combined changes in α-lath thickness, oxygen enrichment, and prior-β grain size. The microstructural changes are due to the differences in the ratio between contouring and hatching laser strategies as the sample size decreases. Changes in the chemical composition is due to an increase in the surface-to-volume ratio as the sample size decreases. Lost of ductility is due to poor surface quality – smaller sections show rougher surfaces – and grain orientations. Finally, these findings are used to develop a set of conceptual design maps of strength and ductility as a function of the component type, thickness, and orientation.

1. Introduction and background

Additive manufacturing (AM) is called to revolutionise the design of engineering components in fields such as space [1], power-generation [2], transport [3,4], and biomedical [5–8]. AM freedom of design allows fabrication complex geometries, thus opening the door to light-weighting of components or structure functionalisation [9–12]. This is

---

* Corresponding author. Escuela Técnica Superior de Ingeniería Aeronáutica y del Espacio (ETSIAE), Universidad Politécnica de Madrid, Plaza Cardenal Cisneros 3, 28040, Madrid, Spain.
E-mail address: daniel.barba@materials.ox.ac.uk (D. Barba).

https://doi.org/10.1016/j.matdes.2019.108235

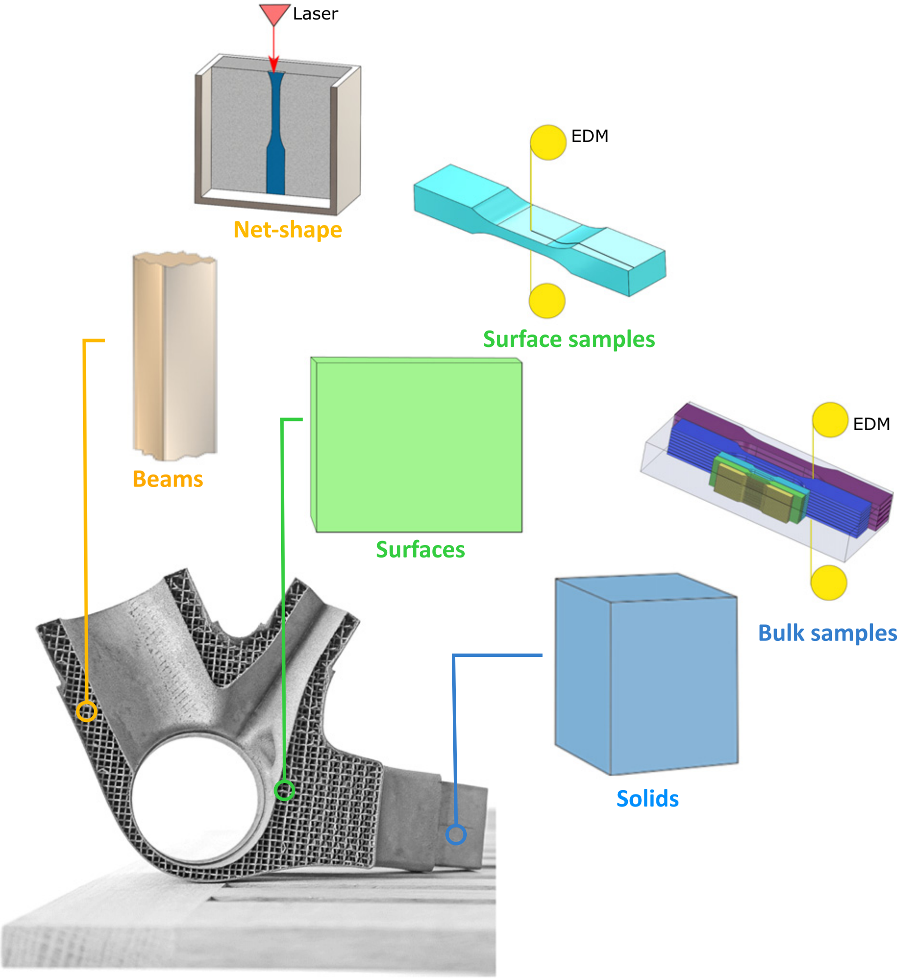

Fig. 1. Different printed structures that can be present in an additive manufactured component and its equivalent in the experimental campaign presented in this paper [51].

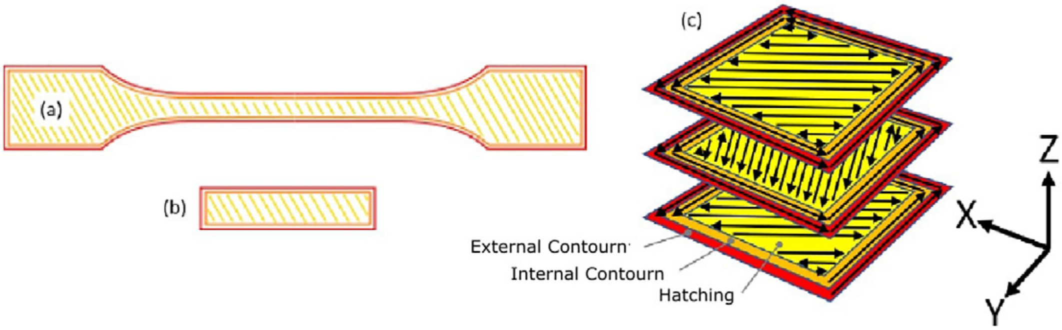

Fig. 2. a) Laser path for the longitudinal plane of an XY type sample; b) laser path for the cross sectional plane of a ZZ type sample; c) detail of the laser paths along the different consecutive planes.

specially the case for metals, where the weight and cost saving opportunity of additive is higher than for other materials such as polymers [13,14]. The structural optimisation allowed by AM translates into the characteristic length of elementals in the manufactured component varying considerably from conventional manufacturing. Characteristic areas of the printed elements can vary from 0.125 mm^2 – representative of biomedical latticed structures – to 18 mm^2 – relevant for light-weight component applications, see Fig. 1. This, combined with different printing parameters and laser orientations relative to the printed geometry,

Table 1
Sample sizes and cross-sectional areas.

Sample	Thickness	Width	Cross area	Gauge length	Surface-volume ratio
A	3 mm	6 mm	18 mm^2	30 mm	1
B	1.5 mm	3 mm	4.5 mm^2	30 mm	2
C	1.0 mm	2 mm	2.0 mm^2	10 mm	3
D	0.5 mm	1 mm	0.5 mm^2	10 mm	6
E	0.25 mm	0.5 mm	0.125 mm^2	10 mm	12

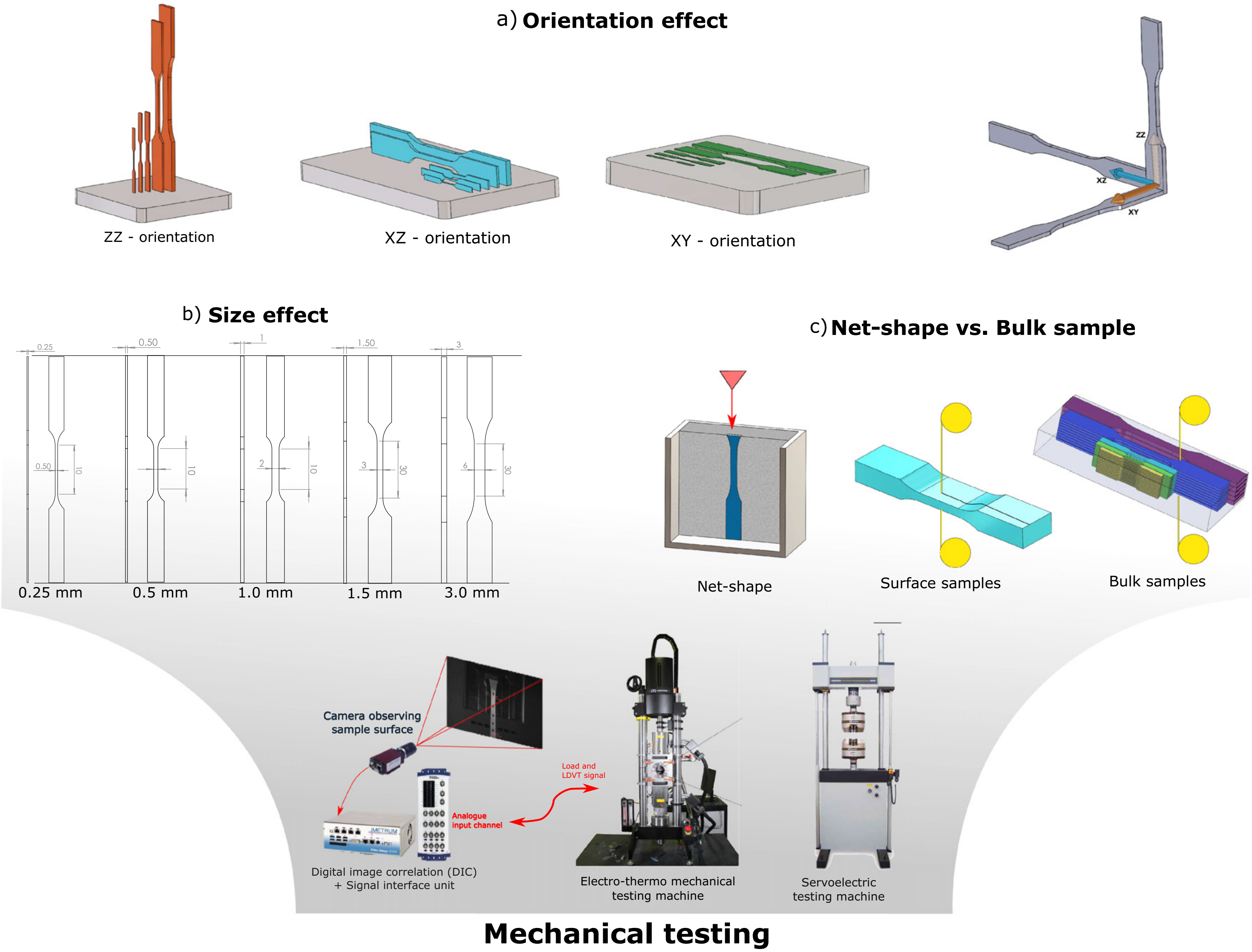

Fig. 3. a) Different orientations conceived in this work to study the effect of build orientation of the samples on the mechanical properties; b) specimen geometries used in this paper for the different sample thickness to study the AM size effect; c) different procedures leading to the final sample geometry to study the differences between net-shape struts, net-shape walls and bulk AM material (extraction of wall and bulk sample by EDM); d) diagram of the mechanical testing method followed in this work: Instron ETMT is used for small size specimens (0.15–1 mm) and Instron servo-electric machine is used for larger size specimens (1.5–3 mm).

Table 2
Complete set of size, orientation, and sample type conditions considered in this work. Symbols: 🔴 refers to ZZ direction, 🔵 refers to XZ orientation and 🟢 refers to XY orientation.

Thickness (mm)	Net-shape	Surface	Bulk	Non-AM
0.25	🔴🔵	🔴🔵🟢	🔴🔵🟢	
0.5	🔴🔵	🔴🔵🟢	🔴🔵🟢	🟢
1	🔴🔵	🔴🔵🟢	🔴🔵🟢	🟢
1.5	🔴🔵	🔴🔵🟢	🔴🔵🟢	
3	🔴🔵	🔴🔵🟢	🔴🔵🟢	

Table 3
AM parameters used for the manufacturing of the tensile samples.

Ti-6Al-4V	Hatch parameters	Border parameters
Layer thickness	30 μm	30 μm
Laser Power	200 W	100 W
Point distance	55 μm	45 μm
Hatch distance	65 μm	65 μm
Exposure time	50 μs	40 μs
Spot size (radius)	35 μm	35 μm

creates property inhomogeneity within the component [15–19]. This integrity heterogeneity is a critical problem for the certification and qualification of additive components. This issue – which remains unsolved – is preventing adoption in high-performance critical applications, *i.e.* aerospace, biomedical, structural. In order to achieve optimal performance of additive components, the size and orientation effect needs to be fully understood.

Ti-6Al-4V is one of the preferred alloys in aerospace applications and biomedical fields [20–23]. The effect of the processing parameters, printing size, and orientation on mechanical properties have been studied extensively [15,24–28]. Similar studies have been carried out to understand their effect on microstructure [25–30] – specially for laser additive manufacturing, *e.g.*, selective laser melting (SLM). This technique offers lot of attractiveness for high performance components due to the high quality of the materials, manufacturing times, and energy efficiency [4]. In order to unleash this performance, one must understand the microstructure that the additive process creates. Due to the large temperature gradients present during the solidification in SLM, an array of columnar β grains are usually formed [15,30–32]. During the fast cooling ($\approx$ 1000 K/s), thin α' martensitic laths (which are metastable) are formed within the prior-β grains. Ti-6Al-4V SLM parts are usually heat treated (HT) to alleviate stress concentrations, and to transform the martensitic $\alpha' \rightarrow \alpha$ – which is stable at RT. During the additive process (and post-process), oxygen enrichment may also occur. This is known as a great strengthener [33,34], but it also affects the

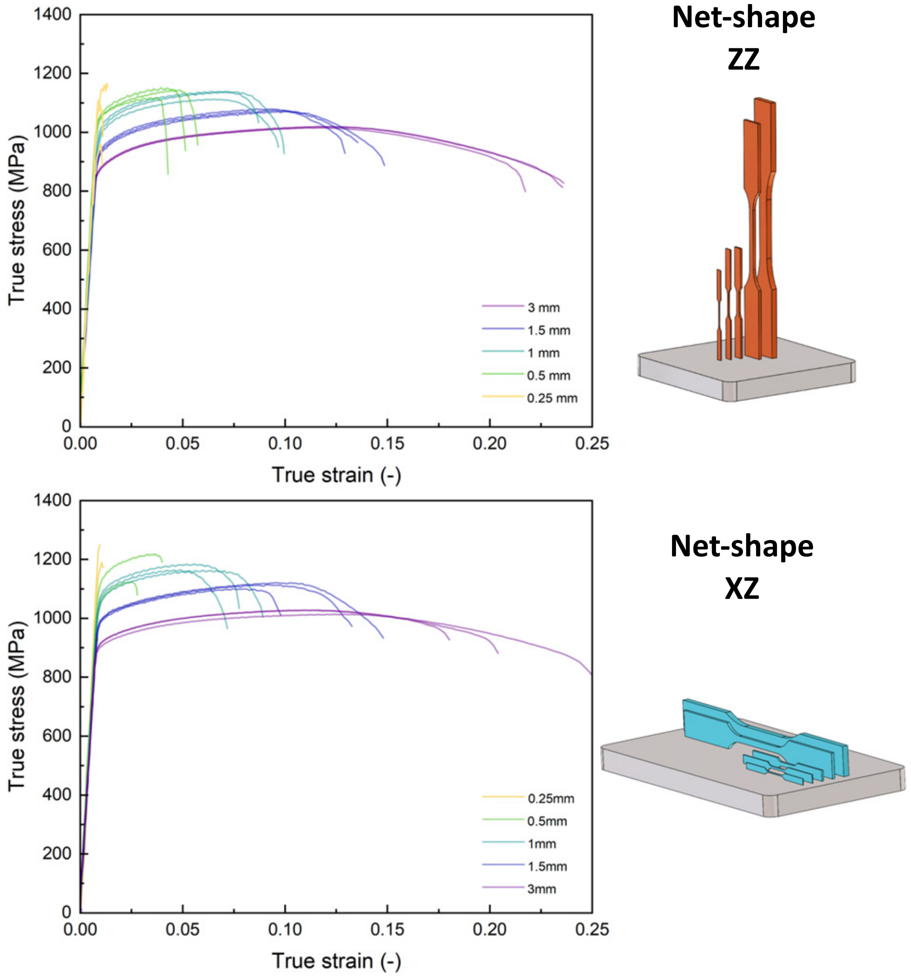

Fig. 4. Stress-strain curves for the case of AM Ti-6Al-4V material of net-shape specimens for ZZ and XZ printed orientations.

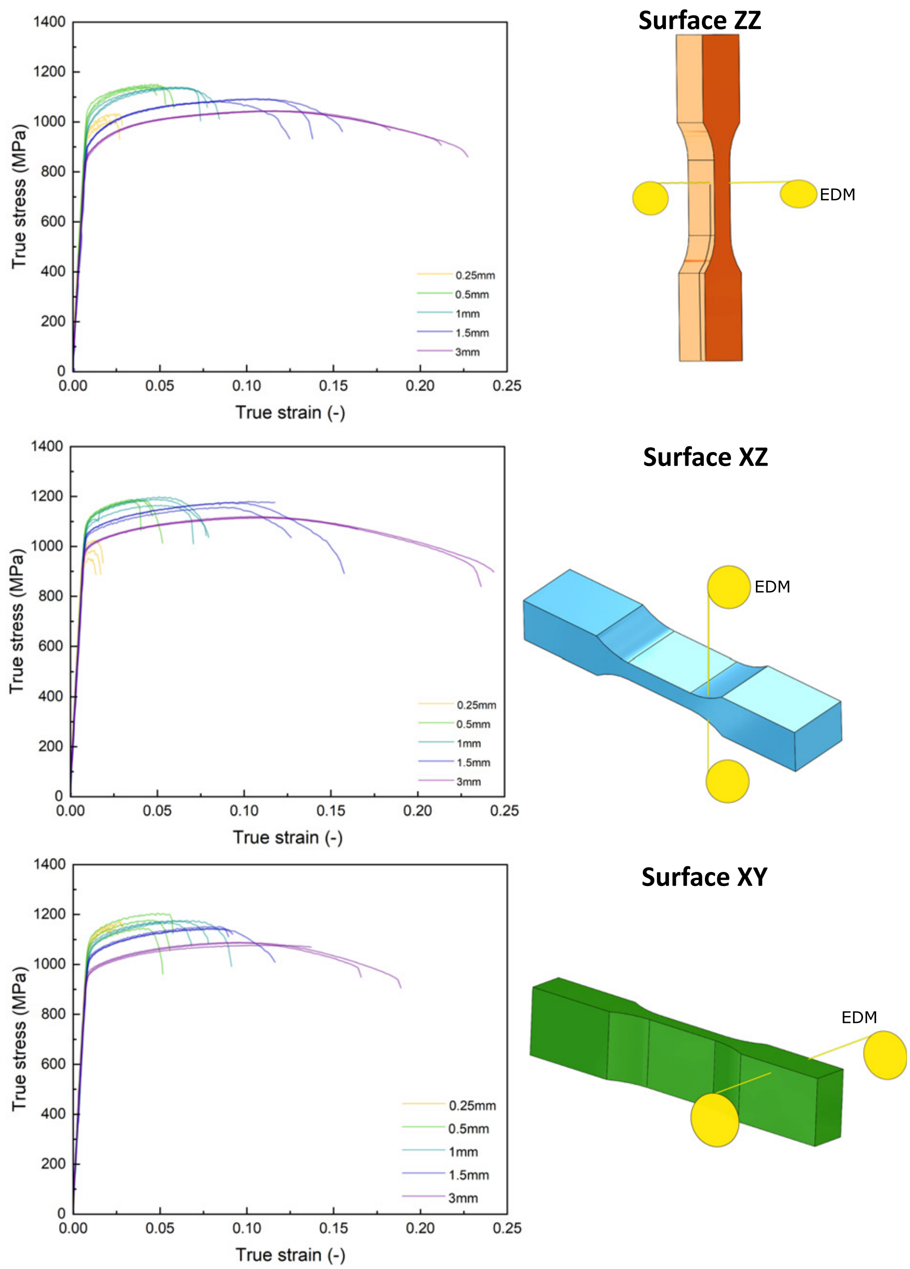

Fig. 5. Stress-strain curves of AM Ti-6Al-4V material for the case of surface-type specimens for ZZ, XZ and XY printed orientations.

ductility. The final properties (*i.e.*, strength, ductility) and anisotropy of the material are determined by the final microstructure, the local chemistry, and the surface quality. The prior-β grain structure and the laths thickness change significantly for different printing sections depending on their vicinity to free surfaces and the orientation of the printed element [15,25,27,28,30]. The oxygen content of the materials can also be affected by the sample geometry and size. These critical aspects are the focus of several efforts in the literature [25,28,33,34].

For example, Antonysamy et al. [30] studied the effect of printed wall thickness and orientation on the structure of prior-β grains in Ti-6Al-4V manufactured by electron beam melting. They found a drastic change of microstructures as the wall thickness decreases from coarse columnar $\langle 001 \rangle_\beta$ grains along the printing direction to a more refined random microstructure in thin walled structures. They linked these changes with the different scanning strategies dominant in each case: *i.e.* hatching in thick structures and contouring in thin structures. Wauthle et al. [27] studied the effect of the printing direction on the mechanical properties of thin lattice structures. They found that Ti-6Al-4V has poorer material properties in horizontal struts. Similarly, elongated β grains along the building direction were found. The preliminary results indicate the rotation of the fibre axis along the strut direction. In both cases, limited information about the changes in the α-lath structures were provided. Zhao et al. [28] studied the effect of the sample thickness and orientation on the mechanical properties of EBM and SLM Ti-6Al-4V. Zhao et al. employed pre-machined samples with diameters between 1.2 and 7 mm. They found better ductility, yield stress and ultimate tensile strength in vertical samples. A slight refinement of the α-lath thickness with the reduction in sample size was also reported. However, the samples were not manufactured net-shape. Finally, Simonelly et al. [15] presented a detailed study of the effect of printing direction on the mechanical properties and microstructure in SLM Ti-6Al-4V. Their results showed an elongated $\langle 001 \rangle$ β grain structure for all orientations. Simonelly et al. also found that the preferred texture in prior-β grains is translated into the fine α laths variant

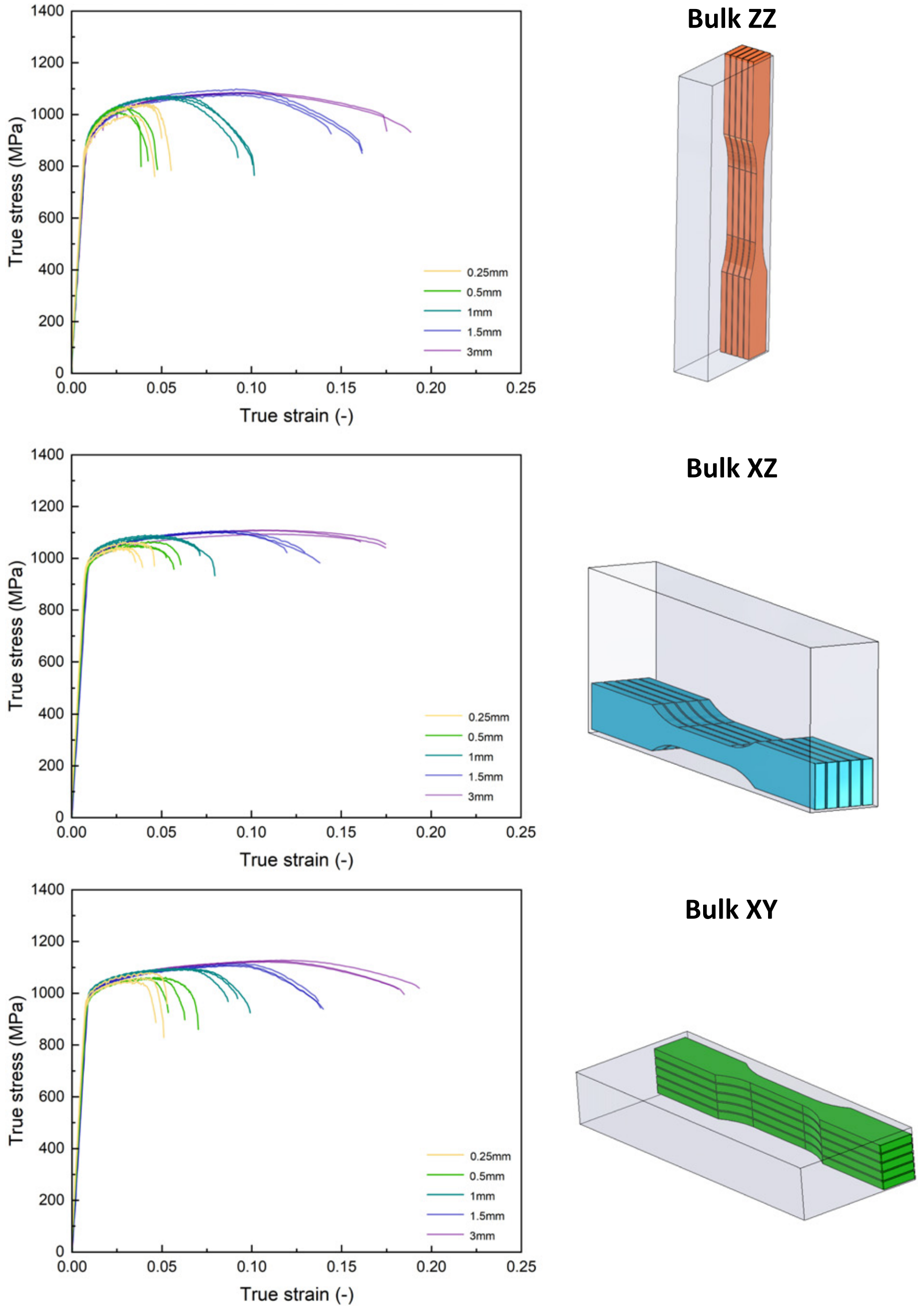

Fig. 6. Stress-strain curves of AM Ti-6Al-4V material for the case of bulk-type specimens for ZZ, XZ and XY printed orientations.

selection process, which was found to affect the mechanical and fatigue properties compared with conventionally manufactured Ti. The ductility of SLM Ti–6Al–4V was found dependent on the build orientation: the horizontal samples had the best tensile properties and the greatest elongation at fracture. These studies (amongst others) are good start point to tackle the challenge. However, none of these provide a holistic view of the process: (*e.g.* obviating mechanical properties [30], neglecting the effect of net-shape parts [28], not including size effects [15–17], lacking of microstructural analyses [18]), or not considering chemical changes [33,34].

With the above in mind, this work present a comprehensive systematic study that includes the effect of print size, print orientation, formed microstructure, local chemical composition, and mechanical properties. More importantly, the influence amongst each other are here connected and rationalised. This work is structured as follows: (i) we design a set of AM testing specimens to quantify the influence of sample size, build orientation, and surface finish (net-shape, surface, and bulk); (ii) we address the mechanical properties of each of the cases in an consistent statistical study; (iii) we characterise the microstructures, chemistry and surface quality of each of the specimens to study the influence of the aforementioned factors; (iv) we make the required connections between design → microstructure, chemistry & surface quality → mechanical properties.

2. Experimental methods

2.1. Specimens for size, orientation and net-shape/bulk effects

In order to study the influence of the different sample geometries and orientations on the mechanical properties the following characteristics are varied and studied in our work:

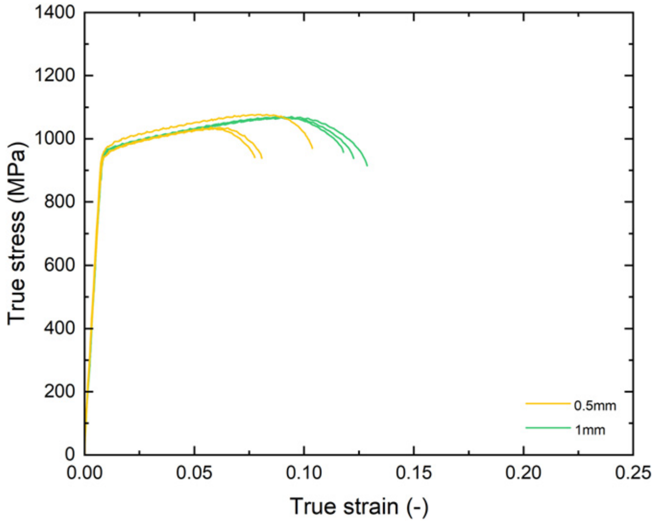

Fig. 7. Stress-strain curves for the case of conventionally manufactured Ti-6Al-4V material.

- **As-printed size:** A systematic study of the effect of the printed sample size on the mechanical properties is performed. Five different sample sizes are considered – see Table 1. These range from a large component representative sample (A: 18 mm^2) to struts representative of thin lattice structures (E: 0.125 mm^2). The five different sample geometries are detailed in Fig. 3b. A summary of the cross-sectional dimensions is provided in Table 1.
- **Build orientation:** The effect of the printing direction is studied by manufacturing the A-E set of samples in three different directions: along the building direction (ZZ), along the building plane with one sample edge on the build plate (XZ) and lying on the horizontal plane (XY) – see diagram in Fig. 3a.
- **Net-shape vs. surface vs. bulk material:** We considered the three different element types present in AM components as stated in Fig. 1. The three case-equivalent samples are: (1) net-shaped specimens (lightweight struts), (2) specimens extracted by electro discharge machining (EDM) from printed blocks (bulk samples) and (3) from semi-net shaped edges (surface or wall samples) as indicated in Fig. 3c.
- **Additively manufactured vs. cast and wrought Ti-6Al-4V:** Finally, additively manufactured Ti-6Al-4V is compared to conventionally manufactured Ti-6Al-4V. Samples with 0.5 and 1 mm thickness are compared (C-D geometry).

To summarise, the whole set of sample conditions considered in this study are presented in Table 2. For the case of net-shape specimens, the orientation XY is not considered due to manufacturing issues on thin horizontal samples (peeling).

2.2. Material and sample manufacturing

All the tested samples were built using a Renishaw AM400 machine with a modulated 200 W ytterbium fibre laser. The power fed into the machine was a plasma atomised Ti-6Al-4V provided by Renishaw. The processing parameters for the additive manufacturing processes were optimised for having highly-dense samples. The parameters used are detailed in Table 3. The effective velocity of the laser can be derived from $v = \frac{\text{point distance}}{\text{exposure time} + \text{travel time}}$. Special care was taken to have an optimal set of parameters which allows for a consistent comparison of the material properties between samples. For the scanning path, a stripe hatching strategy was adopted. Each layer was oriented with a 65° shift from the previous layer. Two contour passes were performed in the free surfaces – the second one using lower energy density laser parameters as shown in Table 3. Schematics of the laser strategy are presented in Fig. 2.

For the case of surface-type samples, large blocks of around 50 mm height with the predefined lateral shape of the samples were manufactured (see Fig. 3c). These pieces were then sliced *via* electro-discharged machining (EDM) to the same geometry of the net-shape specimens shown in Fig. 3b. Finally, for bulk-type specimens, large rectangular blocks of about 75×60×25 mm^3 where additively manufactured (see Fig. 3c). Those were then EDM to the net-shaped geometry. Non-AM testing samples were extracted using EDM from sheets of cast and wrought Ti-6Al-4V (those were taken along the rolling direction).

2.3. Mechanical testing

Tensile tests were conducted on the dog bone specimens presented in Fig. 3b under displacement rate control at a strain rate of $\dot{\varepsilon} = 10^{-2}\mathrm{s}^{-1}$. Small size specimens (thicknesses = 0.25, 0.5 & 1.0 mm) were tested in an Instron electro-thermo mechanical testing machine (ETMT) equipped with a 5 kN load cell. Large size specimens (thicknesses = 1.5 & 3 mm) were conducted in an Instron servo-electric machine equipped with a 100 kN load cell. Digital image correlation (DIC) was used to track the material deformation for all tests and to extract the macroscopic strain of the sample. All tests were performed with the same DIC

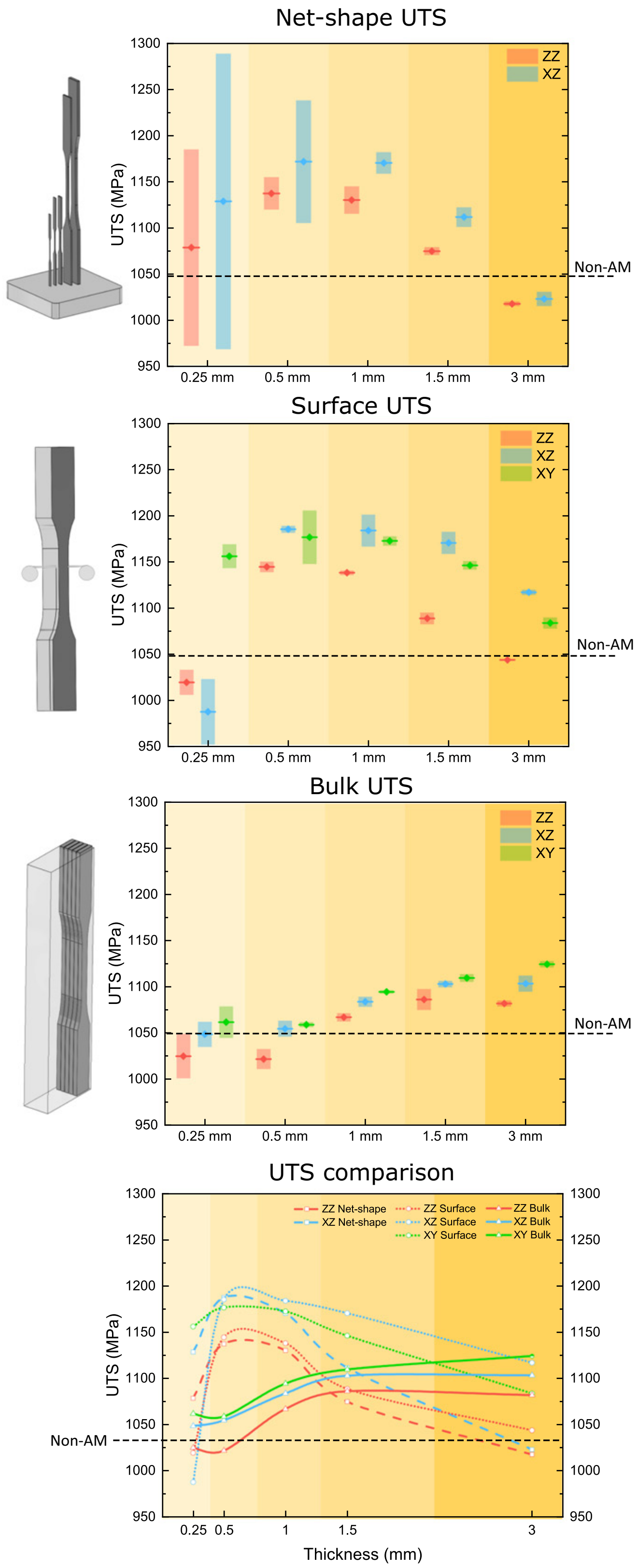

Fig. 8. Ultimate tensile strength (UTS) for the different specimens, orientations and sample sizes tested and overall comparison of the mean UTS values. Bars in the first three graphs represent the standard deviation from 3 repetitions and the central line-dot indicates de mean average UTS value.

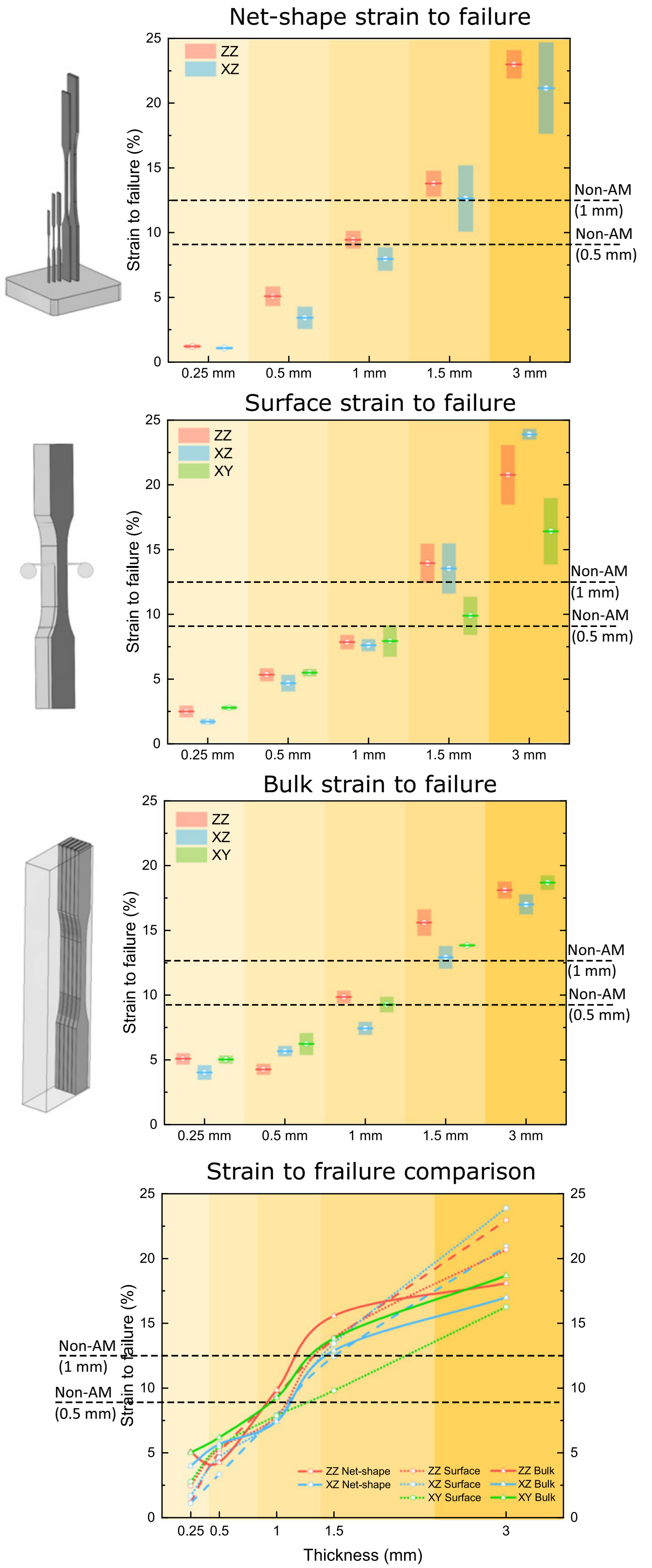

Fig. 9. Strain-to-failure values for the different specimens, orientations and sample sizes tested and overall comparison of the mean strain-to-failure values. Bars in the first three graphs represent the standard deviation from 3 repetitions and the central line-dot indicates de mean average strain-to-failure value.

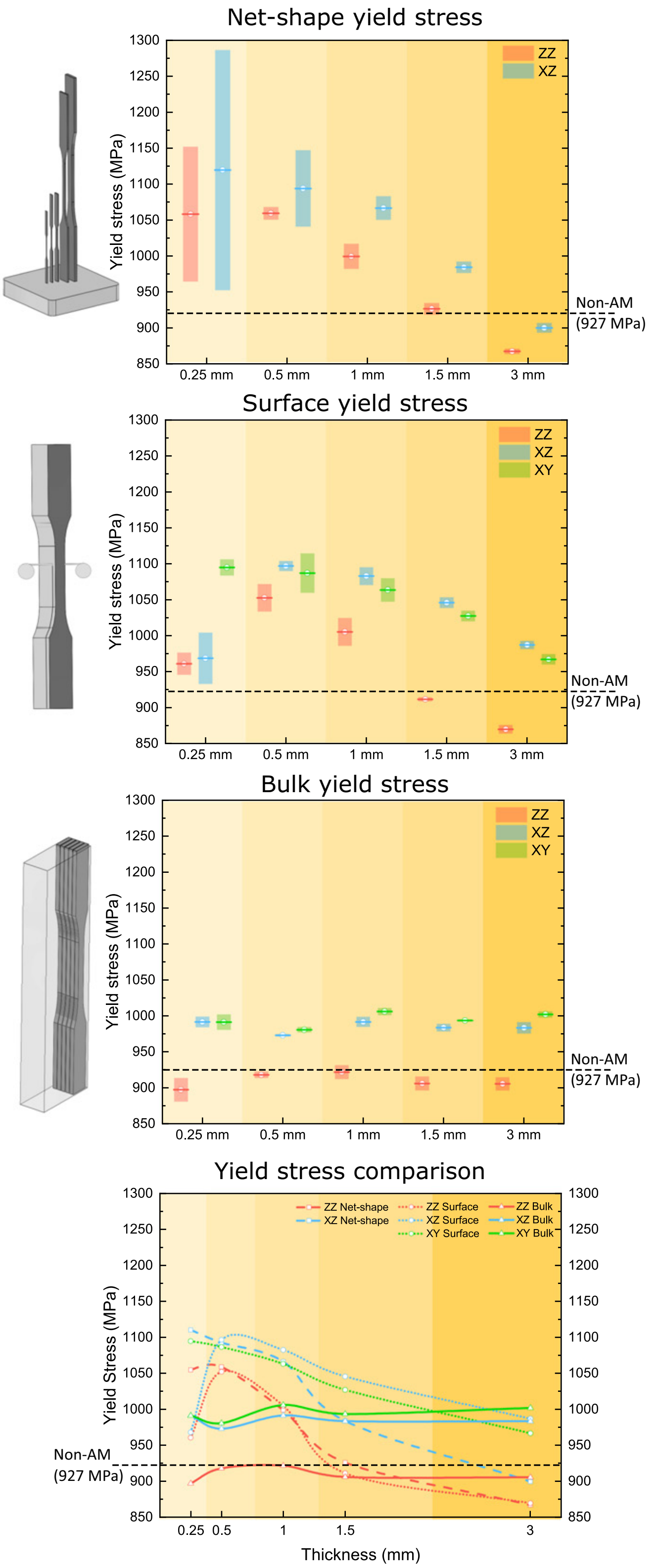

Fig. 10. Yield stress values for the different specimens, orientations and sample sizes tested and overall comparison of the mean UTS values. Bars in the first three graphs represent the standard deviation from 3 repetitions and the central line-dot indicates de mean average yield stress value.

parameters with previously documented good accuracy and repeatability. For consistent comparison, a constant effective gauge length of 10 mm was used in the DIC analysis of all tensile samples. The experimental set-ups are illustrated in 3d.

Surfaces manufactured by EDM (for surface- and bulk-type samples) were polished up to 1200 grit size to assure a good surface finish and to remove the EDM damage layer. Net-shape samples were tested as-manufactured to maintain the

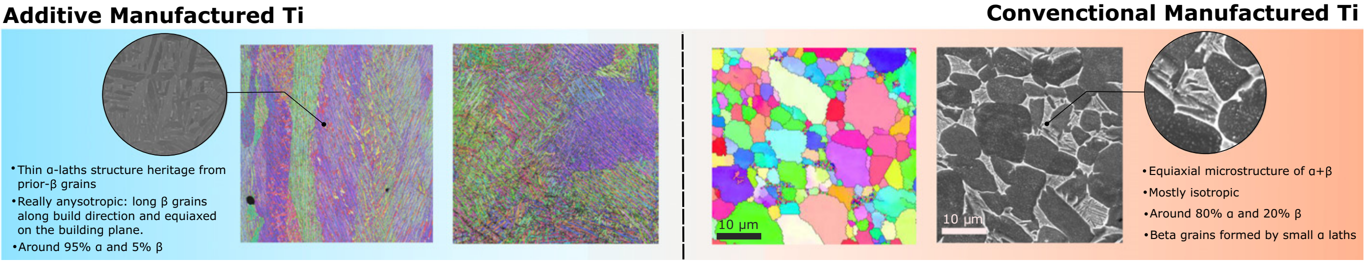

Fig. 11. Different types of Ti-6Al-4V microstructures present in additive manufacturing (left) and conventional manufacturing (right). For AM, the structure is formed by thin α-laths hosted by columnar prior-β grains along the building direction. In CM, the microstructure is composed by a mix of α and β equiaxial grains.

heritage AM microstructure. All the tests were conducted until fracture. Three repetitions of each test condition were performed to assure a consistent statistical study of the mechanical performance of the specimens: a total of 126 specimens were tested. Area of the samples to calculate the stress was obtained by averaging the sample dimensions across cross sectional images of the samples obtained by optical microscopy.

2.4. Microscopic analysis

Metallographic examination of the samples was performed to study the effect of the sample size, the orientation, and the sample type (net-shape, surface or bulk) on the microstructure (α-laths network, prior-β grain structure, and surface roughness).

The α-lath structure was analysed using a JEOL 6500 Field emission gun scanning electron microscope (FEG-SEM) equipped with a backscattered detector. This provided images with phase and orientation contrast. The micrographs were processed afterwards to extract the average α-lath thickness using Image J software [35].

The prior-β grain structure was analysed using a Zeiss Merlin high-resolution FEG-SEM. The SEM is equipped with a Bruker EBSD detector, which was operated at 15 kV accelerating voltage at 15 ms acquisition rate. The microstructure (composed by α-laths) were scanned with a spatial resolution of 620 nm, where the diffraction patterns were stored at 320 × 240 resolution. The collected data was then analysed using an in-house script to reconstruct the prior-β grain structure from the α-lath structure.

Finally, the surface roughness of the samples were characterised using an Alicona optical microscope at x50 augments. The surface roughness property R_a was analysed used the ImageJ Plugin Analyse Stripes [36].

2.5. Chemical analysis

The concentration of oxygen for each of the net-shape specimens was analysed as a function of the sample thickness. A LECO ONH836 Oxygen/Nitrogen/Hydrogen Elemental Analyser was used for this purpose.

3. Results

First, the mechanical results are presented and analysed. After this, the microstructural, chemical, and surface characterisation is presented and commented upon.

3.1. Mechanical results

In the following section, the results obtained from the mechanical testing campaign are presented. First, the effect of the sample size and orientation on the mechanical response are analysed. Secondly, the differences between net-shape, surface and bulk specimens are addressed and compared to the mechanical behaviour of conventionally manufactured Ti-6Al-4V.

3.1.1. Effect of sample size and orientation

The mechanical response of the different sample geometries and sizes are presented in Fig. 4 for net-shape specimens, Fig. 5 for surface-type specimens, and Fig. 6 for bulk-type specimens. Finally, Fig. 7 shows the tensile results obtained for conventional manufactured Ti-6Al-4V (CM-Ti). The whole set of repeats are presented in the graphs.

The summarised values of ultimate tensile strength (UTS), yield strength (YS), and fracture strain are presented in Figs. 8–10. In the following paragraphs, the specific behaviour of each sample types is analysed separately:

- **Net-shape specimens:** The yield strengths presented in Fig. 10 show similar trends for ZZ and XZ directions. A continuous increase of the strength as the sample size decrease is observed. For small size samples (0.25 mm thickness) the strength becomes mostly flat or even decreases presumably due to the effect of the surface damage in high surface-to-volume ratio specimens. This also explains the high scatter observed for small thickness specimens ($t = 0.25$–0.5 mm) when compared with the 1–3 mm specimens. For all the specimens (except for the 3 mm ones), the strength is higher than the one measured for CM-Ti (927 MPa – extracted from 7). Similar trend is observed for the case of the UTS in Fig. 8 but with a more acute final drop of strength for 0.25 mm specimens. Similarly, most of the specimens present a higher UTS than the one measured for CM-Ti (1047 MPa – extracted from 7). For both yield strength and UTS, specimens printed along the XZ direction presented slight-higher strength than the ZZ direction – this is in accordance with other studies in the literature [15,28,37]. This orientation dependence will be further rationalised in Sec. 3.2and it is due to the elongated prior-β grain structure along the ZZ direction. Oppositely to the UTS and yield strength, the strain-to-failure (see Fig. 9) decrease continuously as the sample size decreases. In this case, AM net-shape titanium present worse or equal strains-to-failure than CM-Ti for most cases ($t \leq$ 1.5 mm). The ZZ direction has higher strains-to-failure than the XZ direction. This effect of the orientation infers an effect of the underlying microstructure which will be further discussed in Sec. 3.2.
- **Surface-type specimens:** In this case, it is observed a higher orientation dependence of YS strength than in the net-shape case (Fig. 10). For samples $t > 0.5$ mm, XZ present the highest YS followed by XY and finally, considerably lower, ZZ. This is related to the anisotropy of the β-grains structures as later explain in Sec. 3.2. Conversely, for the case of $t = 0.25$ mm, this tendency inverses – XY presents a higher yield strength than XZ. This might be related to the influence on external defects on horizontal hanging surfaces. Again, the same effect observed for net-shape specimens is spotted here: a higher yield strength as the sample thickness decreases leading to a final plateau or even drop (for ZZ and XZ). Same tendency is observed for the UTS (see Fig. 8), with a final drop of properties for small size specimens being more acute. Both the UTS and the YS present higher ($t = 0.5$, 1.0, 1.5 mm) or roughly equal (0.25, 3 mm) values than CM-Ti. The same orientation effect is observed: ZZ strongest, then XY, and finally XZ. Finally, the strain-to-failure shows the exact same size-effect tendency than for net-shape specimens. Similar values are observed for all directions (Fig. 9).
- **Bulk-type specimens:** Finally, as expected, no size-effect is found on the YS (Fig. 10) of bulk-type samples. The UTS seems to decrease slightly with decreasing size (Fig. 8) – this may be an effect of the high surface-to-volume ratio. Nevertheless, it results minimal when compared to net-shape or surface-type specimens. No significant orientation dependence is observed. The YS and UTS values for bulk-type specimens are in agreement with CM-Ti. The strain-to-failure shows a plateau at low thickness ($t \leq 0.5$ mm). This is different than net-shape and surface-type specimens. The values at high thicknesses ($t \geq 1.5$ mm) are lower than for the two other types of specimens while at lower thickness ($t \leq 0.5$ mm), there is an inversion of the tendency with strains higher than net-shaped and surface-type specimens.

3.1.2. Comparison between AM net-shape, AM surface-type, AM bulk-type titanium, and CM titanium

Finally, the overall differences between the three different types of AM samples and the Non-AM material are analysed. The differences can be observed in the summary plots at the bottom of Figs. 8–10.

- **Yield strength:** Three different regions can be identified; (i) An initial region at large sections ($t \geq 1.5$ mm) where the microstructural refinement in surface and net-shape specimens does not play an important role. This leads to similar yield levels for all the specimen types (net-shape, surface and bulk). For some cases (net-shape) the stress is lower due to the effect of defects on the AM surface; (ii) A second region ($t =$ 0.5–1.5 mm) where the microstructure refinement in net-shape and surface-type samples increase the strength of the material (10–20% higher than bulk); (iii) A third stage ($t = 0.25$ mm) where the large surface-to-volume ratio and number of defects counteract the strengthening effect of the refined structure. Further analysis will be presented in the next sections – these observations will be linked to the microstructure and chemistry.
- **Ultimate tensile strength:** A similar trend is observed with the UTS. In this case, the effect of the AM surface defects on the strength drop is more pronounced than in the YS – because most of those samples fractured during yield.
- **Strain to rupture:** The effect of the sample type is less pronounced when comparing the strain-to-failure. No major difference can be observed in Fig. 9 between net-shape, surface- and bulk-type specimens – specially as the sample thickness decreases.

3.2. Microstructural, chemical & surface characterisation

The changes in mechanical performance arise from microstructural and chemical differences inherited from the additive manufacturing process itself. The microstructure of Ti-6Al-4V changes radically depending if processed by conventional manufacturing methods or additive manufacturing [38–40]. These changes are summarised in Fig. 11. The microstructure of cast and rolled manufactured Ti6Al-4V is usually a bimodal mix of β- and α- grains. The

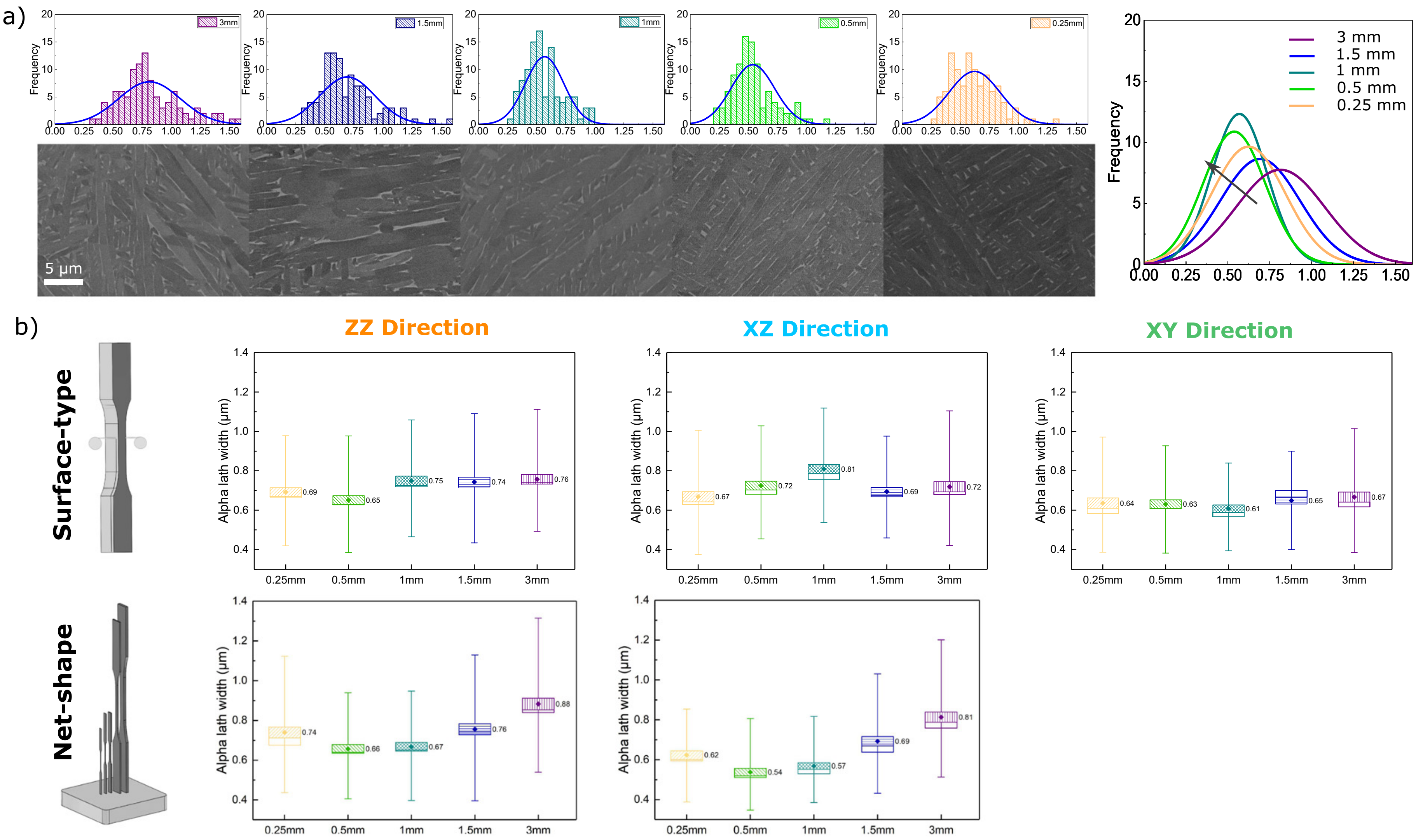

Fig. 12. a) Example of α-lath thickness distribution as a function of the sample thickness for ZZ net shape specimens along with SEM micrographs of the material; b) α-lath thickness as a function of orientation and sample thickness for net-shape and surface specimens.

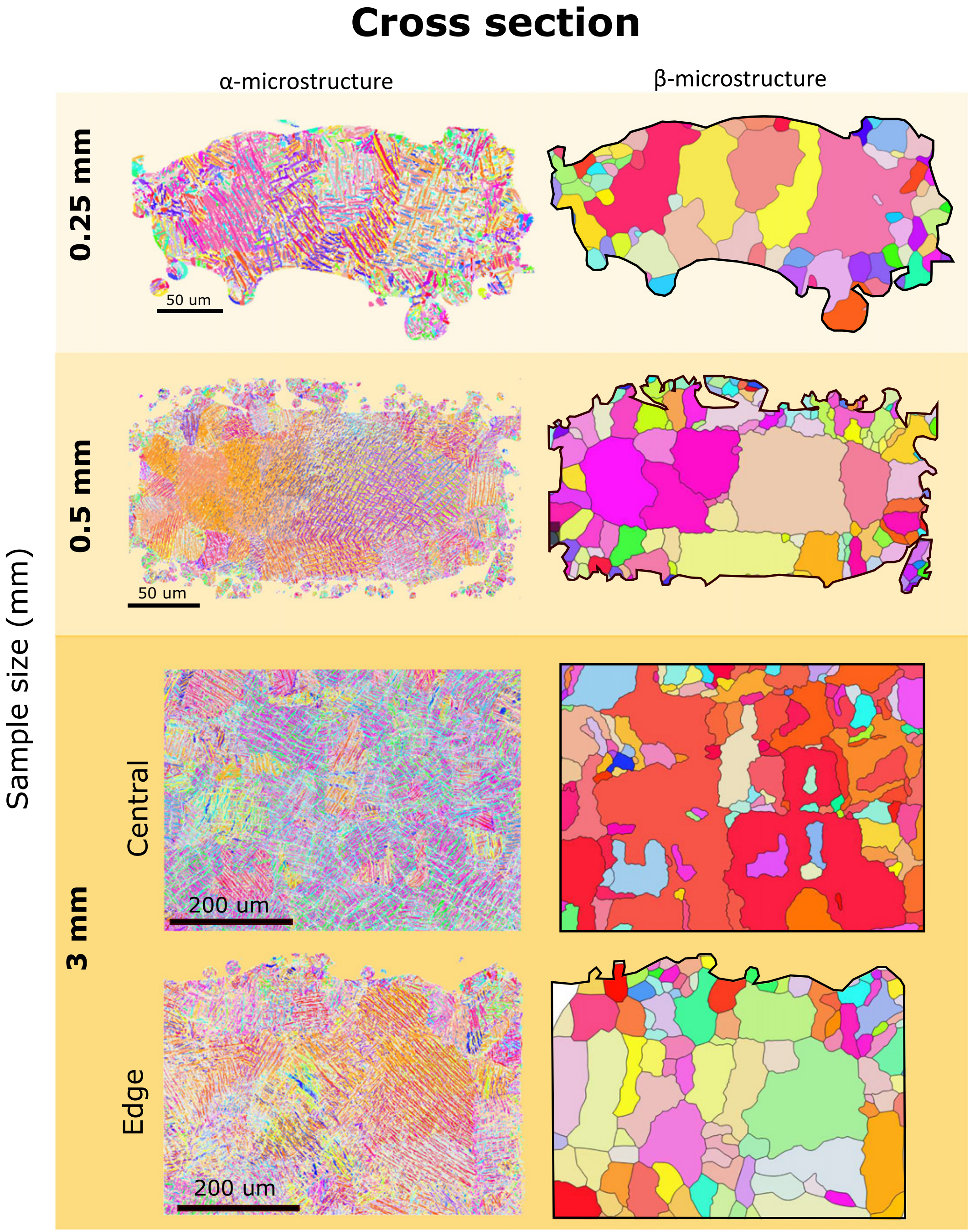

Fig. 13. Cross-sectional EBSD maps of the α-laths microstructure (left) and reconstructed prior-β grain microstructure (right) for the different sample sizes ($t = 0.25$, 0.5 and 3 mm).

conventionally manufactured alloy employed in this paper has 90% of equiaxial α-grains with a mean grain size of approximately 10 μm. The AM microstructure observed in our samples is formed usually by thin α-laths organised in bundles inherited from the prior-β grain structure. This grain structure is usually columnar along the printing direction (ZZ). The size of the α-laths and the prior-β grains are usually connected with the strength of Ti-6Al-4V [26,41]. These two parameters has been found to be strongly influenced by the AM process and sample size. On the other hand, large surface-to-volume ratio produces oxygen enrichment of the samples – both during the AM process and the posterior heat treatment (HT). In solid solution form, O is a known strengthener of Ti alloys [41–43].

With this in mind, the goal of this section is to describe the changes in microstructure, chemistry, and surface quality as a function sample size, orientation and sample type by means of the microstructural characterisation, chemical analysis, and surface examinations. First, the effect of sample orientation, sample size, sample type on the α−laths and prior-β grains microstructures is presented. Secondly, the chemical changes for the different sample sizes are studied using quantitative analysis. Finally, the surface roughness is analysed using optical microscopy and statistical measurements.

3.2.1. α-laths microstructure

The α-laths thickness distribution of net-shape and surface-type specimens has been analysed using stereological statistical analysis. An example of this analysis is presented in Fig. 12a using ZZ net-shape micrographs. For each lath structure captured by the secondary mode in the SEM, a set of 100 α-laths was selected randomly to obtain the lath-thickness statistical distribution. From this distribution, the statistical mean and standard deviations are extracted. These values are then compared to see the effect of the sample thickness, orientation, and surface type on the mean α-lath thickness. A summary of the results is presented in Fig. 12b for net-shape and surface-type specimens. Bulk-type specimens do not show an influence of sample size on lath thickness. CM specimens are not analysed – these do not have α-laths. The following tendencies are found:

- **Net-shape α-lath microstructure:** For net-shape specimens, a common tendency is found: the lath thickness decrease continuously as the size of the sample decreases (up to $t = 0.5$ mm). Then, the lath thickness increases again for $t = 0.25$ mm. This refinement of the α-laths is related to the different cooling rates produced in different

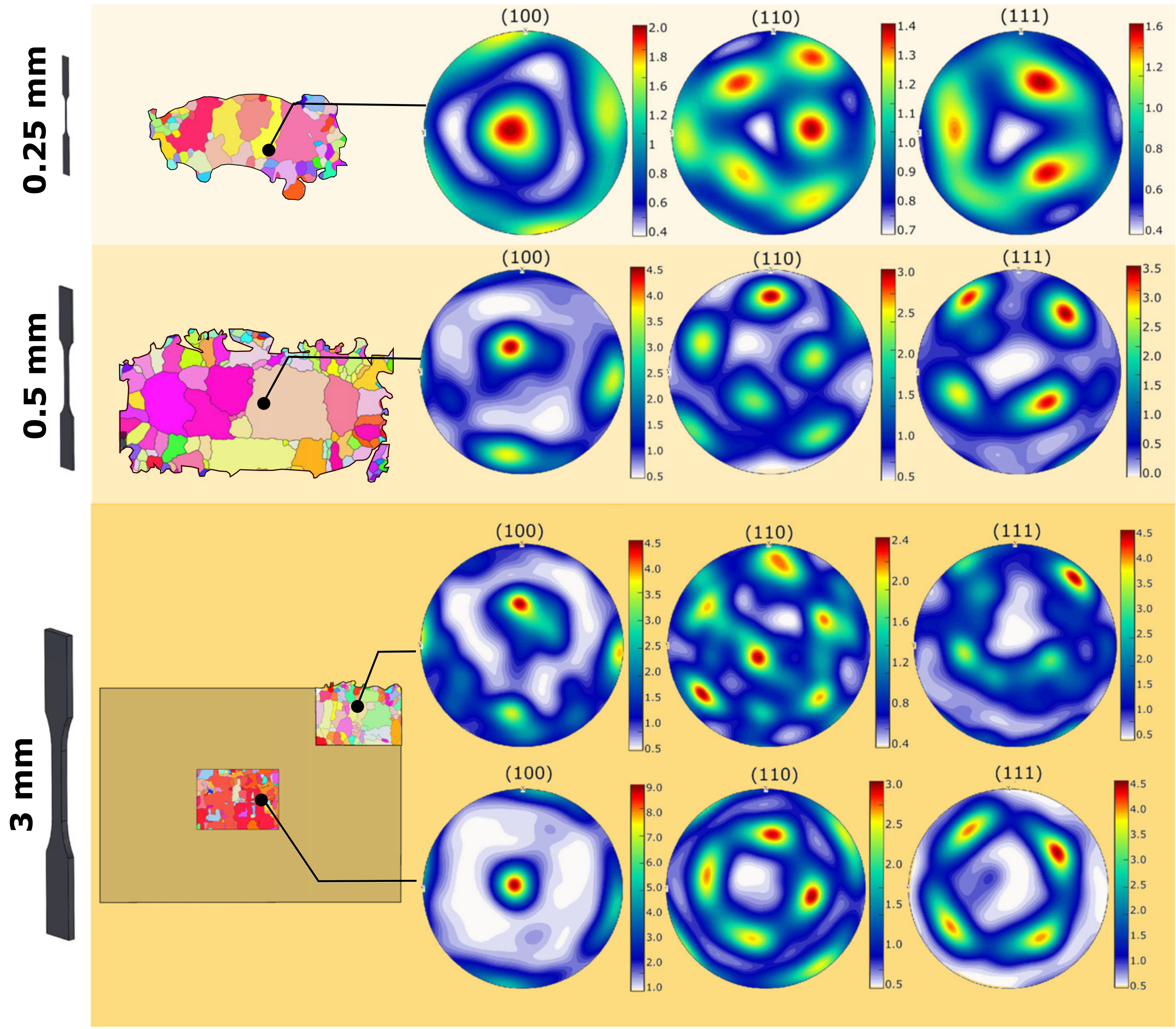

Fig. 14. Orientation distribution function (ODF) pole figures of the prior-β grain structure from the EBSD maps presented in Fig. 13.

size specimens (faster for smaller specimens). The latter increase at $t = 0.25$ mm is believed caused by a different equiaxied prior-β grain structure which set different initial microstructural conditions for α nucleation than for the rest of the cases – 0.25 mm samples were fully manufactured using contour parameters. The direction also influences the lath thickness: XZ direction presents thinner α-laths than the ZZ direction.

- **Surface-type α-laths microstructure:** For surface-type specimens, the tendencies are not that clear. For ZZ direction, the α-lath thickness seems quite flat with a small refinement at $t = 0.5$ mm. For XZ direction, an opposite tendency to net-shape is found: quite flat thicknesses with a small thickening at $t = 0.5$ mm and $t = 1$ mm. Finally, for XY direction, a mostly flat α-laths thickness distribution with a slight refinement as the sample size decrease is observed. The reduction of the size effect on the α-lath thickness when compared to net-shape specimens is due to the change in cooling rates. The overall size of the surface blocks is much larger than the thin net-shape specimens.

These changes in α-lath thicknesses are expected to be driven by the different cooling histories of the different sample sizes and its influence of the prior-β grain microstructure. The latter is analysed next.

3.2.2. Prior-β grain microstructure

The second important microstructural aspect is the structure of prior-β grains. To obtain these microstructural features, the β-grains have been reconstructed from the descendant α-lath structures. This has been done using an in-house script following the transformation theory described in Wagner et al. [44]. In this method, for each individual α-lath, the surrounding α-laths are analysed to find a suitable β parent grain arising from

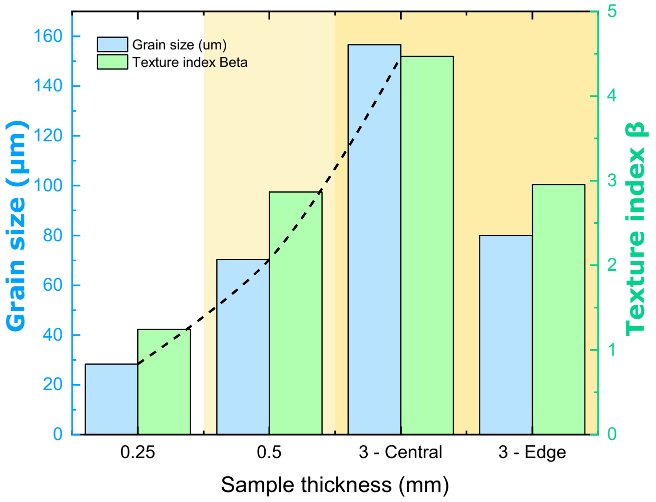

Fig. 15. Prior-β grain size and texture as a function of the sample thickness from the EBSD maps presented in Fig. 13.

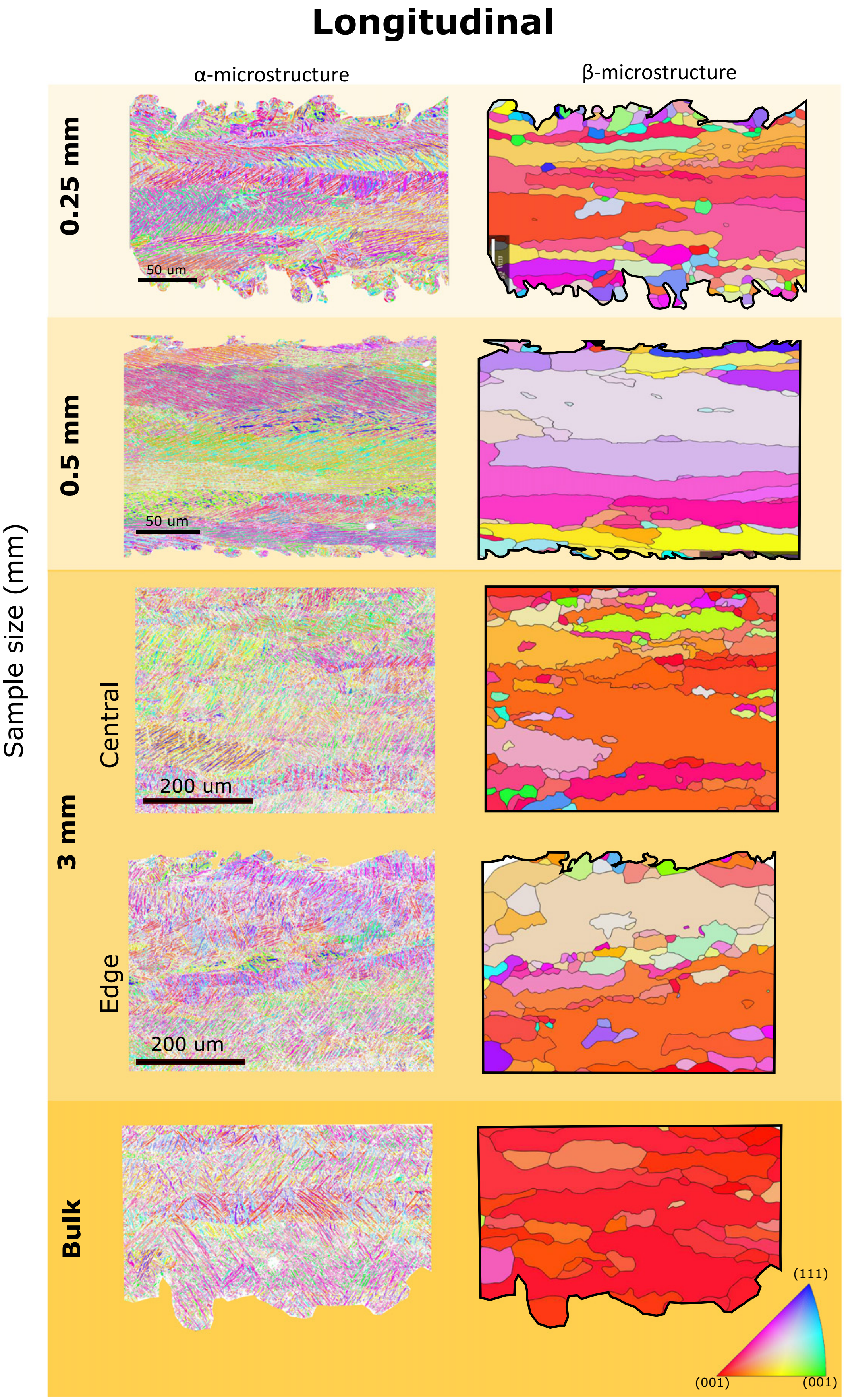

Fig. 16. Longitudinal plane EBSD maps of the α-laths microstructure (left) and reconstructed prior-β grain microstructure (right) for the different sample sizes (t = 0.25, 0.5 and 3 mm).

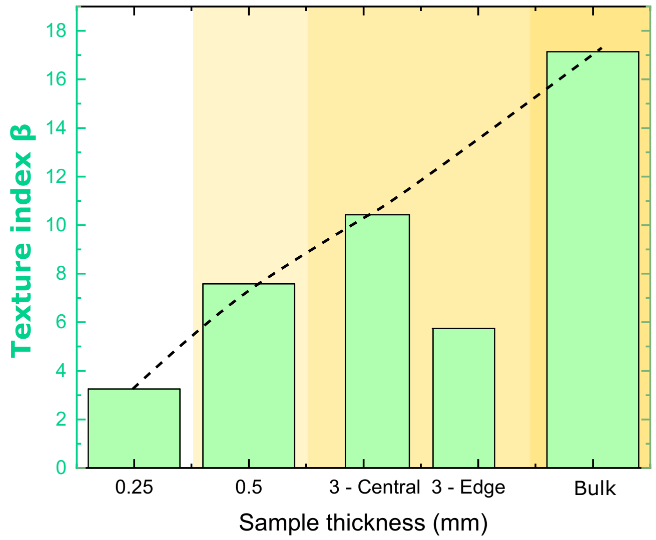

Fig. 17. Prior-β grain size and texture as a function of the sample thickness from the EBSD maps presented in Fig. 15.

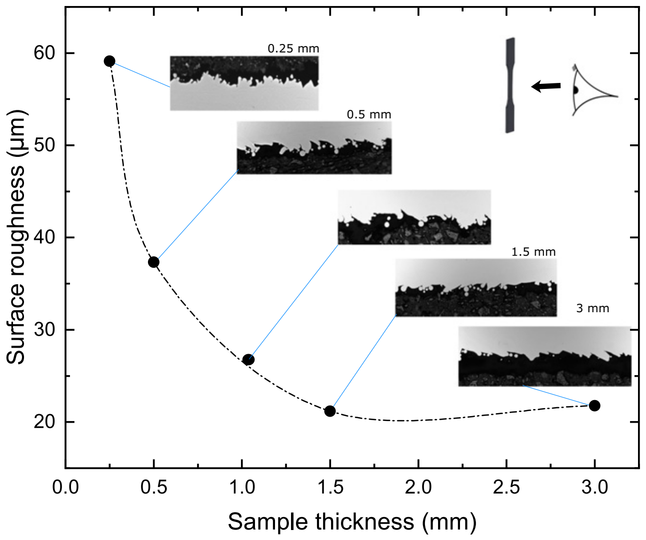

Fig. 19. Surface roughness values along the tensile direction (longitudinal) for the net-shape specimens.

the tensor transformation relationship. If the neighbouring laths share the same β orientation then, these laths are associated to that same β grain. This process continues iteratively along the whole set of laths.

The EBSD maps of the α-laths microstructures along with their prior-β grain reconstructions are presented in Fig. 13 for cross sectional cuts and Fig. 14 for longitudinal cuts. These samples correspond to the net-shape specimens, where larger variations of the microstructure are expected. Three different sample sizes ($t = 0.25$, 0.5 & 3 mm). For the $t = 3$ mm samples, EBSD maps of both core and edge regions were obtained to measure differences induced by the free surface. For cross sectional samples, an additional bulk sample is studied to show the degree of texture found in bulk material. The following particulars are observed:

- **Cross-sectional β-grain microstructures:** The microstructure shows an evolution from a fine-grained arrangement for smaller samples to coarser grains for larger samples. The texture of the grains also evolves from a quite random distribution of orientations for $t = 0.25$ mm to more $\langle 001 \rangle$ textured grains for $t = 3$ mm-central. This characteristic is a direct result of the following process: as the area increases, a central region within the sample gets populated by coarser grains oriented along the build direction (samples $t \geq 0.5$ mm). For larger samples, $t = 3$ mm, the layer of fine randomised grains is constrained to the edge of the sample, leaving most of the sample area with a coarse $\langle 0\,01 \rangle$ textured microstructure. The texturisation of the microstructure as a function of the thickness is further analysed in Fig. 14. Pole figures of the reconstructed β cross section textures are presented. For the build orientation axis (100), a strengthening of the texture from maximum intensity of 2.0 times random at $t = 0.25$ mm to almost 9.5 times random at $t = 3$ mm is observed. The duality of the texture for larger samples is confirmed: *i.e.* $t = 3.0$ mm has a highly textured core surrounded by randomly distributed surface grains. This tendency is further supported by the texture indexes presented in Fig. 15. For each of the cross sectional microstructures, the texture index [45] and the average grain size has been calculated. The results show a direct correlation between prior-β grain size and texture strength. A continuous increase of grain size and texture with sample size is observed. The edge of larger samples ($t = 3$ mm) present a texture level similar to the smaller samples: *i.e.* $t = 0.5$ mm.

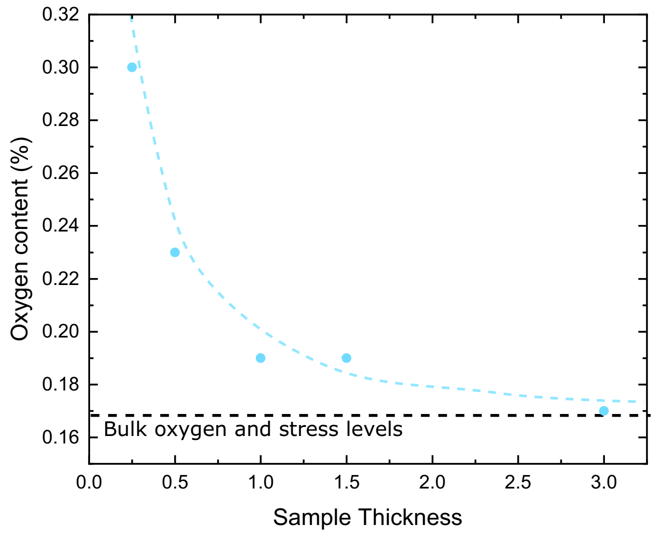

Fig. 18. Oxygen content of the net shape specimens as a function of the sample thickness and comparison with the bulk material values.

- **Longitudinal β-grains microstructures:** The microstructures extracted from net-shape specimens along the longitudinal plane are presented in Fig. 16. All the samples present columnar grain structures along the building direction (Z). The texture index extracted from these maps is presented in Fig. 17. A continuous increase of the texture strength as the sample thickness increases is observed. This is in agreement with the cross-sectional microstructures – reaching x17 random for the case of bulk samples. Moreover, a coarsening of the columnar grain structure can be inferred from the EBSD maps, but larger EBSD maps are needed to confirm this tendency.

The rationalisation of these microstructures and their link to mechanical properties is discussed in the following section.

3.2.3. Chemical analysis: presence of oxygen

Results from the chemical elemental analysis of ZZ net-shaped specimens are presented in Fig. 18. As the sample thickness decreases, the oxygen levels increase. The measured bulk oxygen level (0.168 wt%) is also indicated, it asymptotically converges for large thicknesses. These variations are believed to be key in explaining the different mechanical behaviour observed in the previous section. The strengthening effect of interstitial oxygen is a well-understood phenomenon widely studied in the literature [33,34].

3.2.4. Surface defects analysis

The surface profiles of the ZZ-net samples along their tensile direction are analysed as a function of the sample size. The net-shape specimens are chosen as those will have the highest variability in surface quality. The optical micrographs of the samples edges have been treated and analysed using Image-J [36]. The mean surface roughness (R_a) from each line profile has been computed. The evolution of R_a as a function of the sample size is presented in Fig. 19. There is an inverse correlation between R_a and the sample size: the surface roughness increases with decreasing sample size. This has a direct effect on the mechanical properties of the samples – specially ductility – which will be discussed in the following section. For bulk and surface type samples – where the surfaces were wire EDM and plain polished – no direct effect of roughness is observed.

4. Discussion

In this section, the observed changes in microstructures are connected with the particulars of the additive process. With the processing → microstructure/chemistry connection established, the discussion will focus on the link between microstructure/chemistry → mechanical properties. Finally, both analyses are combined to give a holistic view of the factors which influence the mechanical properties of additively manufactured Ti-6Al-4V.

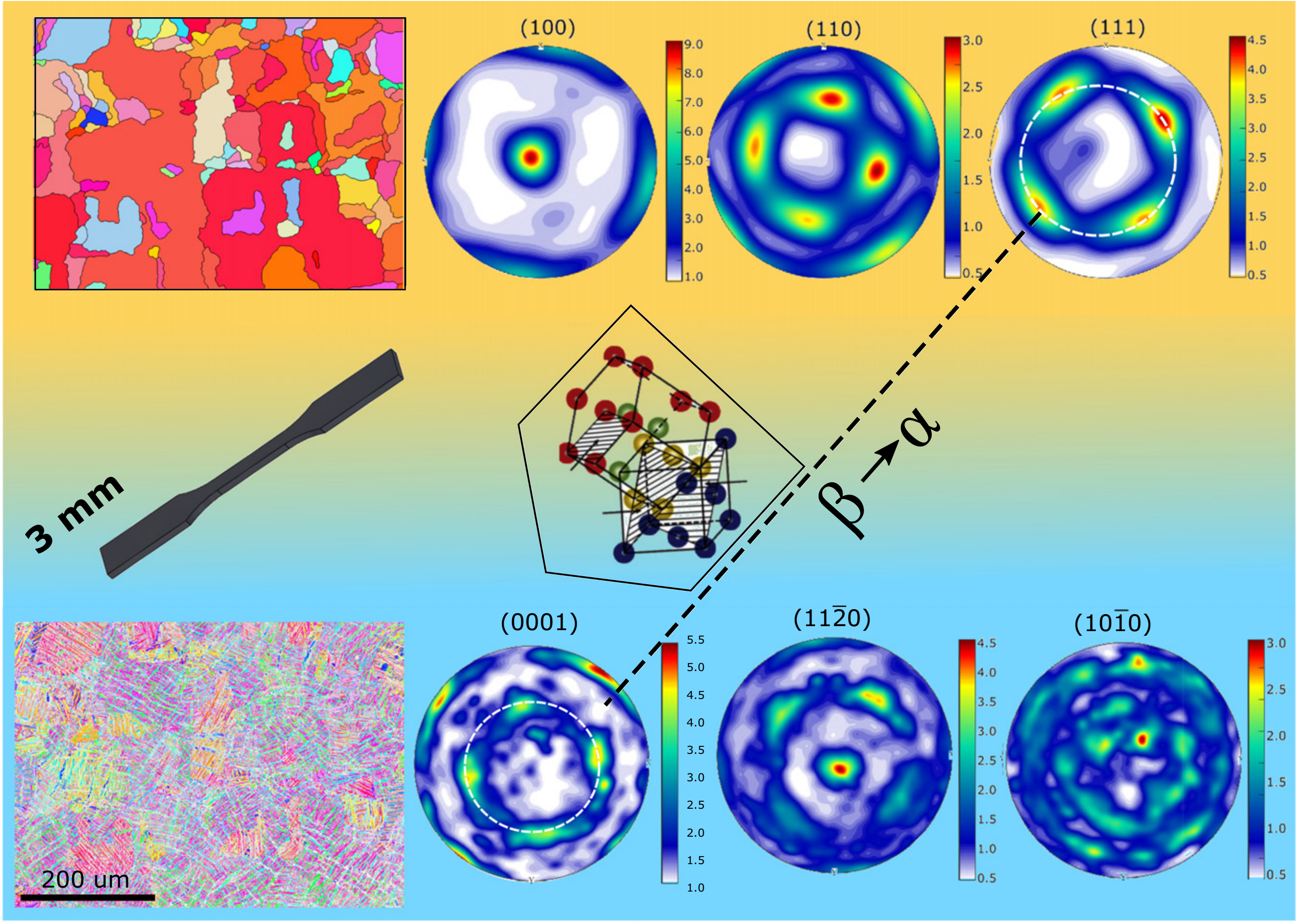

Fig. 20. Digram of the crystal transformation between $\alpha \rightarrow \beta$ and the connection of the texture between both phases.

4.1. Rationalisation of the microstructural and chemical changes

- **Rationalisation of the α-lath microstructures:** The common tendency observed in Fig. 12 is an initial refinement of the lath thickness as the sample size decreases and a final upturn for the smallest thicknesses ($t = 0.25$ mm). The initial refinement is due to two factors: (1) the refinement of the prior-β grain structure and (2) the faster cooling rates as the sample gets smaller. (1) produces a higher grain boundary to grain volume ratio thus leading to a larger number of α-laths nucleation sites per unit volume, thus promoting nucleation over propagation [46,47]. This process leads to a higher number thinner α-laths as the sample size decreases. (2) has been widely studied in the literature, faster cooling rates are related to both a thinner α lath structure and a refinement of the prior-β grain structure [47]. The final increase in the α-lath thickness for samples $t \leq 0.5$ mm can be due to the increase in oxygen. O is a strong α stabiliser [48,49]. This stabilisation can produce the thickening of the α-laths observed in the smallest samples. Samples which are not net-shape do not show this phenomena – the effect of the rapid cooling and prior-β effect is less severe. The influence of the direction of manufacturing in the alpha-lath thickness is believed to be caused by the need of supports in the horizontal samples: Supports will change the heat-history of the sample and promote the nucleation of columnar grains as indicated by Antonysamy et al. [30]. which directly affects the alpha-lath microstructure.

- **Rationalisation of the prior-β microstructures:** Some similarities to the α-lath thickness evolution are found in the case of the prior-β microstructure. Both microstructures are interconnected by the phase-transformation produced during the solidification process (Liquid → β → α'-martensitic) and the posterior heat-treatment (α'-martensitic → α). The crystallographic nature of the $\beta \rightarrow \alpha'/\alpha$ transformation creates a transfer of texture between both phases. This can be observed in Fig. 20, where the pole figures of α and β microstructures are presented. The Burger transformation relationship between both phases – $(110)_\beta || (0001)_\alpha$ – can be observed in the pole figures corresponding to these directions. The texture ring observed along the $(110)_\beta$ is also present along the $(0001)_\alpha$). This provides further proof of the texture transfer.

In terms of the evolution of the prior-β structure with the sample size, the two different types of microstructures observed – (i) fine equiaxial random grains and (ii) textured columnar large grains – are explained by the different processing conditions present in different sample sizes. This is presented schematically in Fig. 21. Two different laser processes are present for each layer in SLM: (i) an initial filling or hatching process consisting of high power (200 W) and long exposure times (50 μs), and (ii) a final contouring process with lower laser power (100 W) and shorter beam pulse time (40 μs). Due to the different solidification paths and temperature gradients produced by the two processes, the resulting microstructures are also different. For the contouring stage, the microstructure produced is usually very fine, more equiaxed and randomised with the grain axis (if certain grain of columnarity is present) at around 45° with respect to the building direction. This is usually aligned with the local temperature gradient as indicated in Fig. 22 [30]. In contrast, the processing conditions of the hatching stage produce highly textured columnar grain structures due to the higher temperature gradients. These grains are produced by the partial re-melting of the previous layers combined with homo-epitaxial growth of the newly melted material. This process is enhanced by the high partition coefficient of the alloying elements (Al & V) present in this alloy. These prevent the creation of new solidification

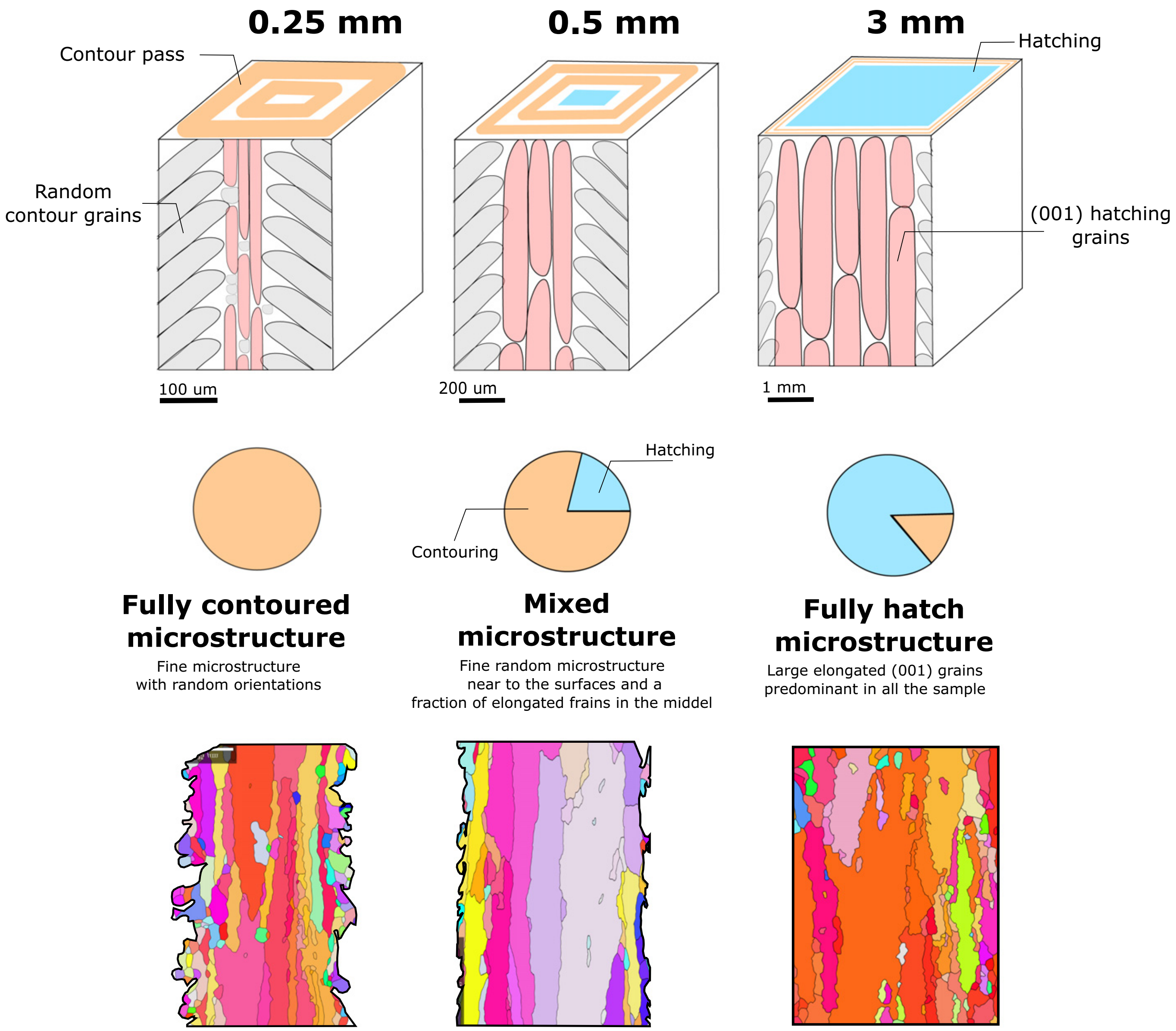

Fig. 21. Diagrams of the different processing conditions for different sample thicknesses and their associated microstructures. Contouring is predominant for thin structures leading to fine random microstructure. Hatching is predominant for thicker samples producing coarse columnar textured grains.

fronts on new layers. This has already been observed in the Electro Beam Melting (EBM) process in Ti-6Al-4V [30]. As indicated in Fig. 22, for large samples, the hatching stage covers most of the area fraction of the sample cross-section. However, for thinner structures ($t <$ 0.5 mm) most of the materials is melted by the contouring passes. This is the reason behind the prior-β microstructure evolution from finer equiaxed grains in thinner samples to large columnar grains observed in larger samples (where most of the sample is produced by hatching). This is indicated schematically in Fig. 22.

- **Rationalisation of the oxygen enrichment:** Finally, oxygen enrichment is due to smaller samples having a higher surface-to-volume ratio. This produces an enhancement of the residual oxygen diffusion present in the environmental chamber during AM process and/or posterior heat treatments. This reinforces the importance of controlling the presence of this element during the whole manufacturing process, specially for thin AM structures such as lattice structures, if one wants to have homogeneous and predictable material properties.

These changes in microstructure and chemistry are now connected with the mechanical properties.

4.2. On the connection between processing → microstructure & chemistry → mechanical properties

- **Microstructure → Mechanical Properties:** The microstructure characteristic size and the texture properties have a direct impact on the strength of the tested material. In this case, the relevant length-scale for the properties is the α-lath thickness (which is intimately related with the prior-β grain size as stated before) together with the texture of the microstructure (heritage from the prior-β grains).

For the first point, there are several studies in the literature that relates directly the strength of the Ti-6Al-4V alloy to the inverse square root of its α-lath thickness [41,46,50]. This correlation is also observed in our study as presented in Fig. 22. This explains part of the strengthening effect.

The second point relates to the texture accounting for part of the orientation dependence of the strength observed in Figs. 8 and 10. This is produced by the anisotropy in the α-lath structure presumably heritage from the anisotropy of the prior-β grain structure. Previous studies in the literature [15,37] have related this textured α microstructure with

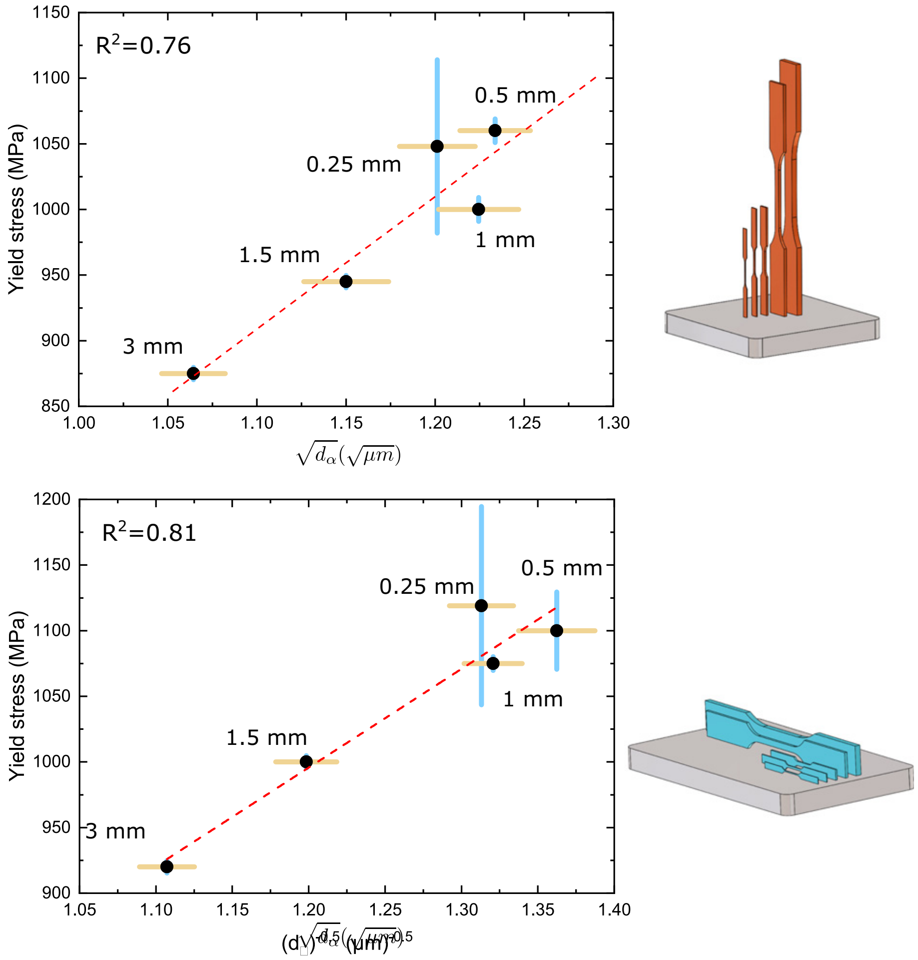

Fig. 22. Correlation between yield strength and the α-lath thickness for the two orientations (ZZ & XZ) of net-shape specimens.

a higher number of well oriented slip α-laths in the vertical direction than in the horizontal build direction, thus producing a higher strength for the latter. This explains the higher values of yield strength and UTS for horizontal directions (XZ and XY) observed in Figs. 8 and 10 – specifically for bulk samples, where the connection is more direct as the surface and oxygen effects are eliminated. On the basis of this theory, no difference between XY and XZ should exist. However, this is not the case. There is a difference in surface-type specimens at small thicknesses ($t = 0.250$mm). This can be caused by presence of support structures for the XY samples which enhances a finer stronger prior-β microstructure as reported before by Antonysamy et al. [30]. As a summary, the typical microstructure size is presented qualitatively as a function of the sample in Fig. 25a.

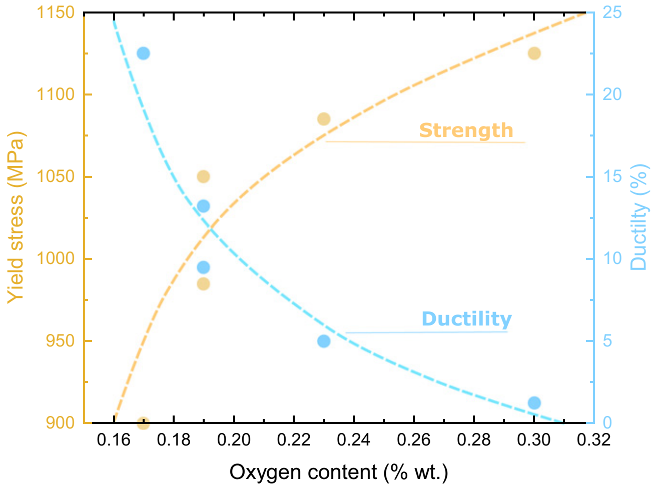

Fig. 23. Yield stress and ductility as a function of the Oxygen content of the samples. There is a direct correlation between oxygen and strength and an inverse correlation between oxygen and ductility.

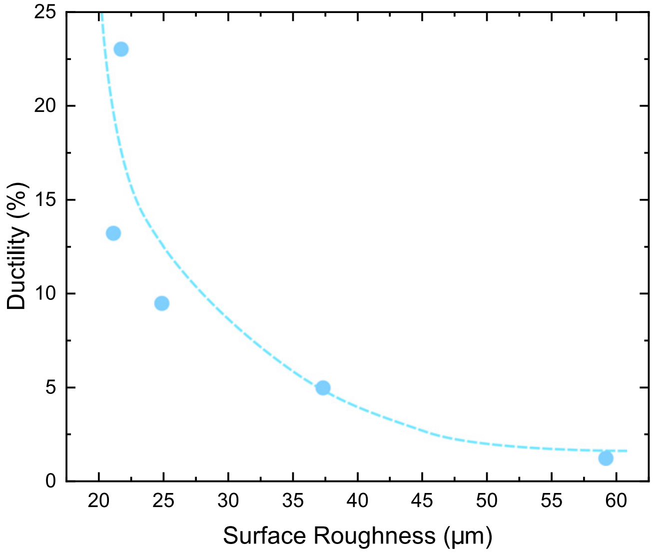

Fig. 24. Correlation between ductility and surface roughness for ZZ net-shape specimens.

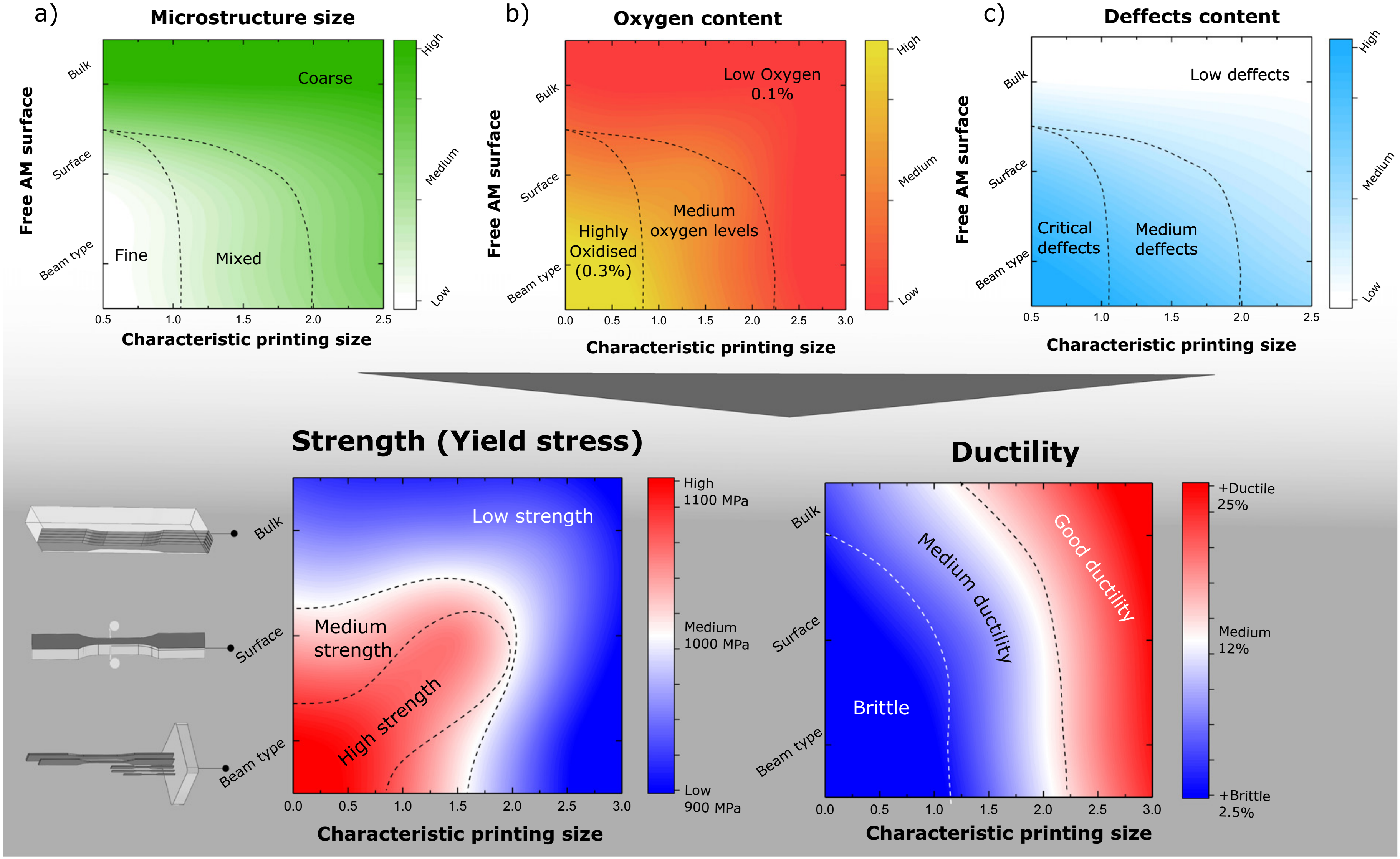

Fig. 25. Microstructural refinement (a), oxygen content (b) and defects contents (c)as a function of the sample size and sample type. The combined effect of these three factors on the strength and ductility is presented in (d).

• **Chemistry → Mechanical Properties** The strong effect of oxygen on the strength and ductility of Ti-6Al-4V is well known [42,43]. In average, strength can increase up to 100 MPa for each 0.01% wt. addition of O. On the other hand, its embrittlement effect can severely impair ductility. This is why certain critical applications limit the O amount. The drop in ductility is also observed in our study as presented in Fig. 23. Conclusively, the oxygen concentration is an important actor in the strengthening and embrittlement of the material as the sample size decreases. As a summary, the oxygen content as a function of the sample size is presented qualitatively in Fig. 25b.

• **Surface → Mechanical Properties:** Finally, the presence of surface defects or surface roughness in the material can induce early failure, thus affecting strongly the ductility and strength of the material. The correlation between the surface roughness and the ductility of the sample is presented in Fig. 24 for net-shaped ZZ specimens. There is a strong loss of ductility as the surface roughness increases – which is higher as the sample gets smaller. This factor is qualitatively presented in Fig. 25c as a function of the sample size and sample type.

The decreasing properties in small samples are found correlated to; (i) the mechanisms of embrittlement and strengthening that O introduces, (ii) the strengthening effect of alpha-lath refinement, (iii) the preferable orientation of the prior-beta grains to the vertical build direction, (iv) the increase in roughness as the sample thickness decreases, and (v) the increase in defect density due to the increase of surface-to-volume ratio as the sample thickness is reduced.

The combined effect of microstructure, chemistry, and surface defects for each geometry and orientation condition produces the observed mechanical behaviour. The combination of all these effects on the strength and ductility is presented qualitatively in Fig. 25. As a summary, for bulk-type or large net-shape & surface-type samples, strength and ductility levels are comparable to conventionally manufactured (CM) Ti-6Al-4V (900 MPa and 15%). For surface-type and net-shape specimens, smaller features ($t \leq 1$ mm) present higher strength values to CM Ti-6A-4V but also lower ductility. Overall, the results of this study present a critical aspect in the design of AM parts: the size and orientation dependent properties of the AM material. No safe design is possible if all these are not taken into account.

5. Conclusions

In this study, the effect of different size and orientation features of additively manufactured Ti-6Al-4V on the mechanical properties, microstructures, chemistry and surface quality have been studied by means of systematic mechanical testing, high-resolution characterisation, and chemical analysis. Several sample sizes have been tested along 3 different build orientations. The effect of bare surfaces has been included in three different scenarios: net-shape, surface-type, and bulk-type specimens. The following conclusions are extracted from this study:

- The mechanical properties of AM Ti-6Al-4V have been measured as a function of sample type, size and orientation. The results show a great influence of the sample size of the strength and ductility of the material as well as an influence of the printing orientation. Generally, for net-shape specimens, the material increases its strength and reduces its ductility as the sample size decreases. Flat properties are observed for bulk-type specimens. In terms of orientations, the ZZ direction has lower strength for all the cases studied.
- The microstructures of the different samples have been studied: specifically the α-lath structure and prior-β grains. For net-shape specimens, the lath thickness initially decreases with the sample size. The refinement of the lath thickness is related to the change in the cooling rate for smaller samples and the prior-β grain size. The prior-β grain structure evolves from fine, equiaxed and randomised microstructure in small samples to a coarse, columnar and highly textured microstructure in large samples. This shift is due to the different contouring-to-hatching ratios for small and bigger samples.
- The levels of oxygen as a function of the sample size have been measured using quantitative chemical analysis. Smaller samples have higher oxygen content due to the higher surface-to-volume ratio. This enrichment happens both during the additive manufacturing and heat-treatment process.
- The surface quality has been quantified as a function of the sample size for net-shape specimens. The surface roughness increases substantially as the sample size decreases and reach a steady value for $t > 1.5$ mm.
- The changes observed in the mechanical properties due to sample size and orientation have been related to changes in microstructure, chemistry, and surface quality. The strengthening observed in net-shape samples as the sample size reduces is due to thinner α-lath microstructure produced by the different processing conditions and a higher oxygen content due to higher surface/volume ratio. The orientation effect (ZZ softer than XZ/XY) is related to the formation of the columnar grains along the ZZ direction and its relation to the presence of a higher density of better oriented α-laths along this direction. The loss of ductility as the sample size decreases is linked to the higher surface-to-volume ratio (thus a higher probability of defects per unit of volume), the oxygen enrichment, and the high surface roughness of the AM process.

CRediT authorship contribution statement

D. Barba: Formal analysis, Writing - original draft. **C. Alabort:** Formal analysis, Writing - original draft. **Y.T. Tang:** Investigation. **M.J. Viscasillas:** Supervision. **R.C. Reed:** Supervision. **E. Alabort:** Formal analysis, Writing - original draft.

Acknowledgements

The authors are thankful for the financial support of OxMet Technologies through the project DJR01450. The authors acknowledge the technical support of Renishaw and Lucy Grainger in this study, and the support provided by Stuart Carter and Jeff Fullerton in the manufacturing of the samples.

References

[1] K. Saha, S. Acharya, C. Nakamata, Heat transfer enhancement and thermal performance of lattice structures for internal cooling of airfoil trailing edges, J. Therm. Sci. Eng. Appl. 5 (2013), 011001.
[2] R. Neugebauer, B. Müller, M. Gebauer, T. Töppel, Additive manufacturing boosts efficiency of heat transfer components, Assemb. Autom. 31 (2011) 344–347.
[3] L. Nickels, Am and aerospace: an ideal combination, Met. Powder Rep. 70 (2015) 300–303.
[4] D. Herzog, V. Seyda, E. Wycisk, C. Emmelmann, Additive manufacturing of metals, Acta Mater. 117 (2016) 371–392.
[5] K. Palka, R. Pokrowiecki, Porous titanium implants: a review, Adv. Eng. Mater. 20 (2015) 1700648.
[6] X. Cheng, S. Li, L. Murr, Z. Zhang, Y. Hao, R. Yang, F. Medina, R. Wicker, Compression deformation behavior of Ti–6Al–4V alloy with cellular structures fabricated by electron beam melting, J. Mech. Behav. Biomed. Mater. 16 (2012) 153–162.
[7] X. Wang, S. Xu, S. Zhou, W. Xu, M. Leary, P. Choong, M. Qian, M. Brandt, Y.M. Xie, Topological design and additive manufacturing of porous metals for bone scaffolds and orthopaedic implants: a review, Biomaterials 83 (2016) 127–141.
[8] F. Bobbert, K. Lietaert, A. Eftekhari, B. Pouran, S. Ahmadi, H. Weinans, A. Zadpoor, Additively manufactured metallic porous biomaterials based on minimal surfaces: a unique combination of topological, mechanical, and mass transport properties, Acta Biomater. 53 (2017) 572–584.
[9] O. Al-Ketan, R. Rowshan, R.K. Abu Al-Rub, Topology-mechanical property relationship of 3D printed strut, skeletal, and sheet based periodic metallic cellular materials, Addit. Manuf. 19 (2018) 167–183.
[10] X. Zheng, H. Lee, T.H. Weisgraber, M. Shusteff, J. DeOtte, E.B. Duoss, J.D. Kuntz, M.M. Biener, Q. Ge, J.A. Jackson, et al., Ultralight, ultrastiff mechanical metamaterials, Science 344 (2014) 1373–1377.
[11] Z. Ozdemir, E. Hernandez-Nava, A. Tyas, J.A. Warren, S.D. Fay, R. Goodall, I. Todd, H. Askes, Energy absorption in lattice structures in dynamics: Experiments, Int. J. Impact Eng. 89 (2016) 49–61.

[12] M.-S. Pham, C. Liu, I. Todd, J. Lertthanasarn, Damage-tolerant architected materials inspired by crystal microstructure, Nature 565 (2019) 305.

[13] W.E. Frazier, Metal additive manufacturing: a review, J. Mater. Eng. Perform. 23 (2014) 1917–1928.

[14] L.J. Gibson, M.F. Ashby, Cellular Solids: Structure and Properties, Cambridge university press, 1999.

[15] M. Simonelli, Y. Tse, C. Tuck, Effect of the build orientation on the mechanical properties and fracture modes of SLM Ti–6Al–4V, Mater. Sci. Eng. A 616 (2014) 1–11.

[16] M. Simonelli, Y.Y. Tse, C. Tuck, On the texture formation of selective laser melted ti-6al-4v, Metall. Mater. Trans. A 45 (2014) 2863–2872.

[17] M. Simonelli, Y. Tse, C. Tuck, Effect of the build orientation on the mechanical properties and fracture modes of SLM Ti–6Al–4V, Mater. Sci. Eng. A 616 (2014) 1–11.

[18] R. Wauthle, B. Vrancken, B. Beynaerts, K. Jorissen, J. Schrooten, J.-P. Kruth, J. Van Humbeeck, Effects of build orientation and heat treatment on the microstructure and mechanical properties of selective laser melted Ti6Al4V lattice structures, Addit. Manuf. 5 (2015) 77–84.

[19] X. Zhao, S. Li, M. Zhang, Y. Liu, T.B. Sercombe, S. Wang, Y. Hao, R. Yang, L.E. Murr, Comparison of the microstructures and mechanical properties of Ti–6Al–4V fabricated by selective laser melting and electron beam melting, Mater. Des. 95 (2016) 21–31.

[20] E. Alabort, D. Barba, R. Reed, Design of Metallic Bone by Additive Manufacturing, Scripta Materialia, 2019.

[21] A. Ataee, Y. Li, M. Brandt, C. Wen, Ultrahigh-strength titanium gyroid scaffolds manufactured by selective laser melting (slm) for bone implant applications, Acta Mater. 158 (2018) 354–368.

[22] E. Alabort, P. Kontis, D. Barba, K. Dragnevski, R. Reed, On the mechanisms of superplasticity in ti–6al–4v, Acta Mater. 105 (2016) 449–463.

[23] B. Cantor, H. Assender, P. Grant, Aerospace Materials, CRC Press, 2015.

[24] T. Machry, D. Eatock, J. Meyer, A. Antonysamy, A. Ho, P. Prangnell, Effect of microstructure on the tensile strength of ti6al4v specimens manufactured using additive manufacturing electron beam process, Powder Metall. 59 (2016) 41–50.

[25] E. Chlebus, B. Kuźnicka, T. Kurzynowski, B. Dybała, Microstructure and mechanical behaviour of ti–6al–7nb alloy produced by selective laser melting, Mater. Char. 62 (2011) 488–495.

[26] W. Xu, M. Brandt, S. Sun, J. Elambasseril, Q. Liu, K. Latham, K. Xia, M. Qian, Additive manufacturing of strong and ductile ti–6al–4v by selective laser melting via in situ martensite decomposition, Acta Mater. 85 (2015) 74–84.

[27] R. Wauthle, B. Vrancken, B. Beynaerts, K. Jorissen, J. Schrooten, J.-P. Kruth, J. Van Humbeeck, Effects of build orientation and heat treatment on the microstructure and mechanical properties of selective laser melted ti6al4v lattice structures, Addit. Manuf. 5 (2015) 77–84.

[28] X. Zhao, S. Li, M. Zhang, Y. Liu, T.B. Sercombe, S. Wang, Y. Hao, R. Yang, L.E. Murr, Comparison of the microstructures and mechanical properties of ti–6al–4v fabricated by selective laser melting and electron beam melting, Mater. Des. 95 (2016) 21–31.

[29] H. Zhao, A. Ho, A. Davis, A. Antonysamy, P. Prangnell, Automated image mapping and quantification of microstructure heterogeneity in additive manufactured ti6al4v, Mater. Char. 147 (2019) 131–145.

[30] A.A. Antonysamy, J. Meyer, P.B. Prangnell, Effect of build geometry on the β-grain structure and texture in additive manufacture of Ti6Al4V by selective electron beam melting, Mater. Char. 84 (2013) 153–168.

[31] M. Simonelli, Y.Y. Tse, C. Tuck, Microstructure of ti-6al-4v produced by selective laser melting, Journal of Physics: Conference Series, vol. 371, IOP Publishing, 2012, 012084.

[32] B. Vrancken, L. Thijs, J.-P. Kruth, J. Van Humbeeck, Heat treatment of ti6al4v produced by selective laser melting: microstructure and mechanical properties, J. Alloy. Comp. 541 (2012) 177–185.

[33] B. Vrancken, S. Buls, J.-P. Kruth, J. Van Humbeeck, Influence of preheating and oxygen content on selective laser melting of ti6al4v, Proceedings of the 16th RAPDASA Conference, 2015.

[34] E. Santos, K. Osakada, M. Shiomi, Y. Kitamura, F. Abe, Microstructure and mechanical properties of pure titanium models fabricated by selective laser melting, Proc. Inst. Mech. Eng. C J. Mech. Eng. Sci. 218 (2004) 711–719.

[35] J. Schindelin, I. Arganda-Carreras, E. Frise, V. Kaynig, M. Longair, T. Pietzsch, S. Preibisch, C. Rueden, S. Saalfeld, B. Schmid, et al., Fiji: an open-source platform for biological-image analysis, Nat. Methods 9 (2012) 676.

[36] J.R. Bickford, Analyze Stripes Plugin, ImageJ, 2013.

[37] J. Yang, H. Yu, Z. Wang, X. Zeng, Effect of crystallographic orientation on mechanical anisotropy of selective laser melted ti-6al-4v alloy, Mater. Char. 127 (2017) 137–145.

[38] H. Rafi, N. Karthik, H. Gong, T.L. Starr, B.E. Stucker, Microstructures and mechanical properties of ti6al4v parts fabricated by selective laser melting and electron beam melting, J. Mater. Eng. Perform. 22 (2013) 3872–3883.

[39] L. Thijs, F. Verhaeghe, T. Craeghs, J. Van Humbeeck, J.-P. Kruth, A study of the microstructural evolution during selective laser melting of ti–6al–4v, Acta Mater. 58 (2010) 3303–3312.

[40] J.L. Warwick, N.G. Jones, I. Bantounas, M. Preuss, D. Dye, In situ observation of texture and microstructure evolution during rolling and globularization of ti–6al–4v, Acta Mater. 61 (2013) 1603–1615.

[41] G. Jia, The Effect of Oxygen Content on the Tensile Properties of SLMed Ti6Al4V Alloy, 2017.

[42] Q. Yu, L. Qi, T. Tsuru, R. Traylor, D. Rugg, J. Morris, M. Asta, D. Chrzan, A.M. Minor, Origin of dramatic oxygen solute strengthening effect in titanium, Science 347 (2015) 635–639.

[43] A. Kahveci, G. Welsch, Effect of oxygen on the hardness and alpha/beta phase ratio of ti-6a1-4v alloy, Scr. Metall. 20 (1986) 1287–1290.

[44] L. Wagner, M. Wollmann, Titanium and Titanium Alloys', Structural Materials and Processes in Transportation, 2013 151–180.

[45] R. Hielscher, H. Schaeben, A novel pole figure inversion method: specification of the mtex algorithm, J. Appl. Crystallogr. 41 (2008) 1024–1037.

[46] I. Ghamarian, B. Hayes, P. Samimi, B. Welk, H. Fraser, P.C. Collins, Developing a phenomenological equation to predict yield strength from composition and microstructure in β processed ti-6al-4v, Mater. Sci. Eng. A 660 (2016) 172–180.

[47] T. Broderick, A. Jackson, H. Jones, F. Froes, The effect of cooling conditions on the microstructure of rapidly solidified ti-6al-4v, Metall. Trans. A 16 (1985) 1951–1959.

[48] H. Ding, G. Nie, R. Chen, J. Guo, H. Fu, Influence of oxygen on microstructure and mechanical properties of directionally solidified ti–47al–2cr–2nb alloy, Mater. Des. 41 (2012) 108–113.

[49] M. Yan, M. Dargusch, T. Ebel, M. Qian, A transmission electron microscopy and three-dimensional atom probe study of the oxygen-induced fine microstructural features in as-sintered ti–6al–4v and their impacts on ductility, Acta Mater. 68 (2014) 196–206.

[50] S. Semiatin, T. Bieler, The effect of alpha platelet thickness on plastic flow during hot working of ti–6al–4v with a transformed microstructure, Acta Mater. 49 (2001) 3565–3573.

[51] B. Cycles, https://bastion-cycles.com/ 2019.